Radiometric flow in periodically patterned channels: fluid physics and improved configurations

Ali Lotfian[1] and Ehsan Roohi[1],†

[1]High Performance Computing (HPC) Laboratory, Department of Mechanical Engineering,
Ferdowsi University of Mashhad, 91775-1111, Mashhad, Iran

With the aid of direct simulation Monte Carlo (DSMC), we conduct a detailed investigation pertaining to the fluid and thermal characteristics of rarefied gas flow with regard to various arrangements for radiometric pumps featuring vane and ratchet structures. For the same, we consider three categories of radiometric pumps consisting of channels with their bottom or top surfaces periodically patterned with different structures. The structures in the design of the first category are assumed to be on the bottom wall and consist of either a simple vane, a right-angled triangular fin or an isosceles triangular fin. The arrangements on the second category of radiometric pumps consist of an alternating diffuse–specular right-angled fin and an alternating diffuse–specular isosceles fin on the bottom wall. The third category contains either a channel with double isosceles triangular fins on its lowermost surface or a zigzag channel with double isosceles triangular fins on both walls. In the first and the third categories, the surfaces of the channel and its structures are considered as diffuse reflectors. The temperature is kept steady on the horizontal walls of the channel; thus, radiometric flow is created by subjecting the adjacent sides of the vane/ratchet to constant but unequal temperatures. On the other hand, for the second category, radiometric flow is introduced by specifying different top/bottom channel wall temperatures. The DSMC simulations are performed at a Knudsen number based on the vane/ratchet height of approximately one. The dominant mechanism in the radiometric force production is clarified for the examined configurations. Our results demonstrate that, at the investigated Knudsen number, the zigzag channel experiences maximum induced velocity with a parabolic velocity profile, whereas its net radiometric force vanishes. In the case of all other configurations, the flow pattern resembles a Couette flow in the open section of the channel situated above the vane/ratchet. To further enhance the simulations, the predictions of the finite volume discretization of the Boltzmann Bhatnagar–Gross–Krook (BGK)–Shakhov equation for the mass flux dependence on temperature difference and Knudsen number are also reported for typical test cases.

Key words: rarefied gas flow

† Email address for correspondence: e.roohi@ferdowsi.um.ac.ir

1. Introduction

The history of the radiometer dates back to 1874 when the first radiometer was designed and built by the chemist Sir William Crookes (Crookes 1874). The radiometer consisted of thin vanes blackened on the one side and whitened on the other. The vanes are generally contained within a partially evacuated glass bulb that provides a rarefied environment. Once exposed to sunlight, the vanes start rotating such that black sides retreat from sunlight and light sides advance. Since the development of the device by Crookes, researchers have been interested either in understanding or in exploiting this phenomenon (Ketsdever *et al.* 2012).

With the advent of micro-electromechanical systems (MEMS) and the associated fabrication technologies, there is a renewed interest in thermally driven (Vargo *et al.* 1999; Aoki *et al.* 2001; Aoki, Degond & Mieussens 2009; Bond, Wheatley & Goldsworthy 2016; Chen *et al.* 2016) and radiometric flows (Taguchi & Aoki 2012, 2015) as radiometers could work as Knudsen pumps for gas transport without any moving parts (Baier *et al.* 2017), microactuators (Gimelshein *et al.* 2011*a*; Strongrich *et al.* 2017), small satellite and spacecraft attitude control devices (Nallapu, Tallapragada & Thangavelautham 2017) and high-altitude propulsion systems (Cornella *et al.* 2012).

Even though some configuration variants have been suggested during recent decades, the primary interest of researchers was in Crookes-based designs (Ketsdever *et al.* 2012; Taguchi & Aoki 2012, 2015; Baier *et al.* 2017). Previous works suggested a few ways to enhance the radiometric force through making holes in the vane, that is, creating a series of sub-vanes located above one another or through edge geometry modification by using a slanted edge geometry (Gimelshein *et al.* 2011*a*,*b*). Research showed that a radiometer with sub-vanes produces more force per radiometer mass than a single-plate radiometer with the same active area. Recently, Shahabi *et al.* (2017) demonstrated that the working principle of a ratchet channel with mixed diffuse and specular reflection boundary conditions on the ratchet surface proposed by Donkov *et al.* (2011) is the same as that of radiometric flow.

With this background in mind, in the current study, we seek to present and assess alternative configurations for the radiometric pumps with periodically structured surfaces and enhanced operational performance and compare them to the original configuration considered in Donkov *et al.* (2011), Shahabi *et al.* (2017). Here, we propose three categories of planar channel radiometric pumps with bottom (and top) surface(s) periodically structured with vane or sawtooth configurations. The first category comprises channels with a standard Crookes radiometer vane, right-angled triangular fin and isosceles triangular fin. The second category considers right-angled triangular and isosceles triangular ratcheting walls with different reflection characteristics (specular diffusive) on both sides. The third category reports a channel with double isosceles triangular fins and a channel with double isosceles triangular fins on both walls (hereby called a zigzag channel). As realizing specular reflection is challenging on actual surfaces, the idea behind the designs in the first and third categories is to use diffusive walls but create the radiometric force by setting different temperatures on the adjacent sides of the vanes or fins. With the aid of direct simulation Monte Carlo (DSMC) and a discrete unified gas-kinetic scheme (DUGKS), the structure of the fluid and thermal fields, as well as force characteristics of the proposed configurations, are described.

2. Methods

2.1. *DSMC method and solution set-up*

Direct simulation Monte Carlo (DSMC) is a molecular-based approach for treating the Boltzmann equation. The Boltzmann equation is defined as:

$$\frac{\partial f}{\partial t} = D[f] + Q[f, f_*], \tag{2.1}$$

where $f = f(\boldsymbol{\xi}, \boldsymbol{x}, t)$ or f_* is the velocity distribution function of particles with velocity $\boldsymbol{\xi}$ and operators D and Q are operators describing the particle convection and binary interactions taking the forms:

$$D = -\boldsymbol{\xi} \cdot \nabla, \tag{2.2}$$

$$Q = \iiint (f'_* f' - f_* f) B(g, \boldsymbol{\theta}) \, \mathrm{d}\Omega(\boldsymbol{\theta}) \, \mathrm{d}\boldsymbol{x}_*, \tag{2.3}$$

where a prime indicates the post-collision distribution functions, $B(g, \boldsymbol{\theta})$ depends on the intermolecular potential, $\boldsymbol{\theta}$ is a unit vector expressing the variation of the particle velocity owing to an intermolecular collision, g is the relative molecular velocity and $\mathrm{d}\Omega$ is a solid angle element in the direction of $\boldsymbol{\theta}$.

To obtain a solution for the Boltzmann equation at time t_{k+1}, the standard DSMC method uses the following splitting scheme applied to the discrete velocity distribution function known at time t_k,

$$f[t_k + \delta t, \boldsymbol{x}(t_k), \boldsymbol{\xi}(t_k + \delta t)] = S_Q^{\delta t, h}\{f[t_k, \boldsymbol{x}(t_k), \boldsymbol{\xi}(t_k)]\}, \tag{2.4}$$

$$f[t_k + \delta t, \boldsymbol{x}(t_k + \delta t), \boldsymbol{\xi}(t_k + \delta t)] = S_D^{\delta t}\{f[t_k + \delta t, \boldsymbol{x}(t_k), \boldsymbol{\xi}(t_k + \delta t)]\}, \tag{2.5}$$

where δt is the time step, and operators $S_Q^{\delta t, h}$ and $S_D^{\delta t}$ are the DSMC numerical algorithms approximating the collision and free molecular motion terms in the Boltzmann equation, respectively.

In DSMC, intermolecular collisions are effectuated for particles localized in cells or subcells. Particle velocities are updated during intermolecular and molecule-surface interactions. We use a recent variant of the original DSMC solver (Scanlon *et al.* 2010) released in OpenFOAM 2.4.0 plus Micro and Nano Flows for Engineering codes, i.e. OpenFOAM-2.4.0-MNF (White *et al.* 2018). The aforementioned DSMC solver was validated for a wide range of rarefied fluid flow simulations (White *et al.* 2013; Palharini *et al.* 2015). Intermolecular collisions are simulated using a variable-hard-sphere (VHS) collision model, and the Larsen–Borgnakke internal energy redistribution model is used for diatomic gases.

Collisional pairs are selected according to the standard no-time-counter (NTC) collision method, for more details see Roohi & Stefanov (2016), Roohi *et al.* (2018). For diffusive walls, particle velocities are sampled from a Maxwellian velocity distribution function at surface temperature. In all the simulations reported in this work, we set 50 particles per cell (PPC) on average. The maximum cell dimensions, Δx and Δy, are chosen to be approximately 0.1λ–0.2λ. The simulation time step is set to be much smaller than the minimum of the transit time (δt_{tr}) and the mean collision time (δt_{coll}). Our particle number, cell size and time step independence tests provided in appendix A show that the chosen PPC, cell size and time step are more than sufficient to guarantee PPC/grid/time step independent DSMC solutions.

Transient adaptive subcells (TAS) are employed so that subcell sizes are automatically adjusted to a pre-specified number of particles per subcell (PPSC), here, PPSC = 2. This ensures that collision partners are selected within a region much smaller than the local mean free path (Su *et al.* 2010). As the number of simulated particles per cell is large enough and fine cells are used, the chance of repeated collisions is very low (Stefanov 2011; Akhlaghi, Roohi & Stefanov 2018). The sample size, gathered after steady state is achieved and used to compute reported force, mass flux and fluid properties, was at least 2×10^6 per cell. Details of cell size and time step in all of the cases are provided in appendix A.

2.2. *Discrete unified gas-kinetic scheme (DUGKS)*

Discrete unified gas-kinetic scheme (DUGKS) (Guo, Wang & Xu 2015; Zhu, Chen & Guo 2017) is a deterministic finite-volume scheme for the discrete velocity Boltzmann model equation. Here, DUGKS is also used to solve rarefied flow in a few vane/ratchet configurations. Compared with DSMC, DUGKS is more computationally efficient for low-speed or near-continuum flow problems. The governing equation is the Boltzmann equation with the Shakhov collision model, that reads (Zhu & Guo 2017*a*):

$$\frac{\partial f}{\partial t} + \boldsymbol{\xi} \cdot \nabla f = \frac{p}{\mu}(f^S - f), \tag{2.6}$$

where p is the pressure, μ is the viscosity coefficient and $p/\mu = 1/\tau$, where τ is the relaxation time. The Shakhov equilibrium distribution function f^S is given by the Maxwell distribution function f^M plus a heat flux correction term, that is:

$$f^S = f^M \left[1 + (1 - Pr)\frac{\boldsymbol{c} \cdot \boldsymbol{q}}{5pRT}\left(\frac{c^2}{RT} - 5\right)\right], \quad f^M = \frac{\rho}{(2\pi RT)^{3/2}} \exp\left(-\frac{c^2}{2RT}\right), \tag{2.7a,b}$$

where Pr is the Prandtl number, R is the specific gas constant and $\boldsymbol{c} = \boldsymbol{\xi} - \boldsymbol{U}$ is the peculiar velocity where $\boldsymbol{U}$ is the fluid velocity. For diatomic nitrogen, Pr was set at approximately 0.7. Macroscopic variables such as density, velocity, internal energy, heat flux and pressure tensor can be calculated by taking moments of the distribution function, e.g.

$$\left.\begin{array}{l} \rho = \int f \, \mathrm{d}\boldsymbol{\xi}, \quad \rho\boldsymbol{U} = \int \boldsymbol{\xi} f \, \mathrm{d}\boldsymbol{\xi}, \quad \rho E = \frac{1}{2}\int \xi^2 \, \mathrm{d}\boldsymbol{\xi}, \\ \boldsymbol{q} = \frac{1}{2}\int \boldsymbol{c} c^2 f \, \mathrm{d}\boldsymbol{\xi}, \quad \boldsymbol{p} = \int \boldsymbol{\xi}\boldsymbol{\xi} f \, \mathrm{d}\boldsymbol{\xi}, \end{array}\right\} \tag{2.8}$$

where E is the total energy.

For two-dimensional problems, the dependence of the distribution function on the z-direction velocity was removed by introducing reduced distribution functions, that is:

$$\Phi = \begin{bmatrix} g \\ h \end{bmatrix} = \int_{-\infty}^{\infty} \begin{bmatrix} 1 \\ \xi_z^2 \end{bmatrix} f(\boldsymbol{\xi}, \boldsymbol{x}, t) \, \mathrm{d}\xi_z. \tag{2.9}$$

Integrating the modified Boltzmann equation over the range $[-\infty, \infty]$ and noting that $\partial\Phi/\partial z = 0$ gives:

$$\frac{\partial\Phi}{\partial t} + \xi_x\frac{\partial\Phi}{\partial x} + \xi_y\frac{\partial\Phi}{\partial y} = -\frac{p}{\mu}[\Phi - \Phi^S], \tag{2.10}$$

where $\Phi^S = [g^S, h^S]^T$ and:

$$g^S = g^M \left[1 + (1 - Pr) \frac{\boldsymbol{c} \cdot \boldsymbol{q}}{5pRT} \left(\frac{c^2}{RT} - 4 \right) \right], \quad (2.11)$$

$$h^S = h^M \left[1 + (1 - Pr) \frac{\boldsymbol{c} \cdot \boldsymbol{q}}{5pRT} \left(\frac{c^2}{RT} - 2 \right) \right] RT, \quad (2.12)$$

$$g^M = \frac{\rho}{2\pi RT} \exp\left(-\frac{c^2}{2RT} \right). \quad (2.13)$$

The discrete unified gas-kinetic scheme (DUGKS) is the numerical procedure used to solve the modelled two-dimensional Boltzmann equation. The scheme is an explicit finite-volume approach for the discrete velocity Boltzmann model equation. First, the model equation is discretized in velocity space with two-dimensional discrete velocity points $\{\boldsymbol{\xi}_\alpha, \alpha = 1, 2, \ldots, M\}$,

$$\frac{\partial \Phi_\alpha}{\partial t} + \xi_{\alpha,x} \frac{\partial \Phi_\alpha}{\partial x} + \xi_{\alpha,y} \frac{\partial \Phi_\alpha}{\partial y} = -\frac{p}{\mu}[\Phi_\alpha - \Phi_\alpha^S] \equiv \Omega_\alpha, \quad (2.14)$$

where Φ_α and Φ_α^S are the distribution function and equilibrium distribution function, respectively, with discrete velocity $\boldsymbol{\xi}_\alpha$. The above equation is then discretized in the space with a cell centred finite-volume technique as follows:

$$\Phi_{\alpha,k}^{n+1} - \Phi_{\alpha,k}^n + \frac{\delta t}{|V_k|} \mathcal{F}_{\alpha,k}^{n+1/2} = \frac{\delta t}{2}[\Omega_{\alpha,k}^{n+1} + \Omega_{\alpha,k}^n], \quad k = \{1, 2, \ldots, N\}, \quad (2.15)$$

where $\Phi_{\alpha,k}^n$ is the cell averaged value of Φ_α of cell k at time t^n, $|V_k|$ is the volume of the cell k, N is the total number of cells and δt is the time step. The flux $\mathcal{F}_{\alpha,k}^{n+1/2}$ is computed as:

$$\mathcal{F}_{\alpha,k}^{n+1/2} = \sum_1 \boldsymbol{\xi}_\alpha \cdot \boldsymbol{S}_{k,l} \Phi_{\alpha,k,l}^{n+1/2}, \quad (2.16)$$

in which:

$$\Phi_\alpha^{n+1/2}(\boldsymbol{x}_f) - \Phi_\alpha^n(\boldsymbol{x}_f - \boldsymbol{\xi}_\alpha \delta t/2) = \delta t/4[\Omega_\alpha^{n+1/2}(\boldsymbol{x}_f) + \Omega_\alpha^n(\boldsymbol{x}_f - \boldsymbol{\xi}_\alpha \delta t/2)], \quad (2.17)$$

where $\boldsymbol{S}_{k,l}$ is the surface vector of face l of cell k, and $\Phi_{\alpha,k,l}^{n+1/2}$ is the face centred distribution function of face l at the middle time step. The detailed algorithm of the DUGKS can be found in Guo *et al.* (2015).

The advantages of the DUGKS are due to its deterministic nature and a particular construction of the distribution flux at cell interfaces; these techniques make it efficient for low-speed and near-continuum flows, respectively. Here, we will use DUGKS to evaluate the dependence of the induced flow on the temperature difference and Knudsen number in two typical cases. A version of DUGKS implemented in the framework of the OpenFOAM package is utilized (Zhu *et al.* 2017).

We performed a study considering various physical and discrete velocity grid sizes as well as quadrature rules for the numerical integration of the moments. The results are summarized in appendix B. According to the results reported in therein, details of the simulations set-up for all the DUGKS cases reported in this work were chosen, see appendix B.
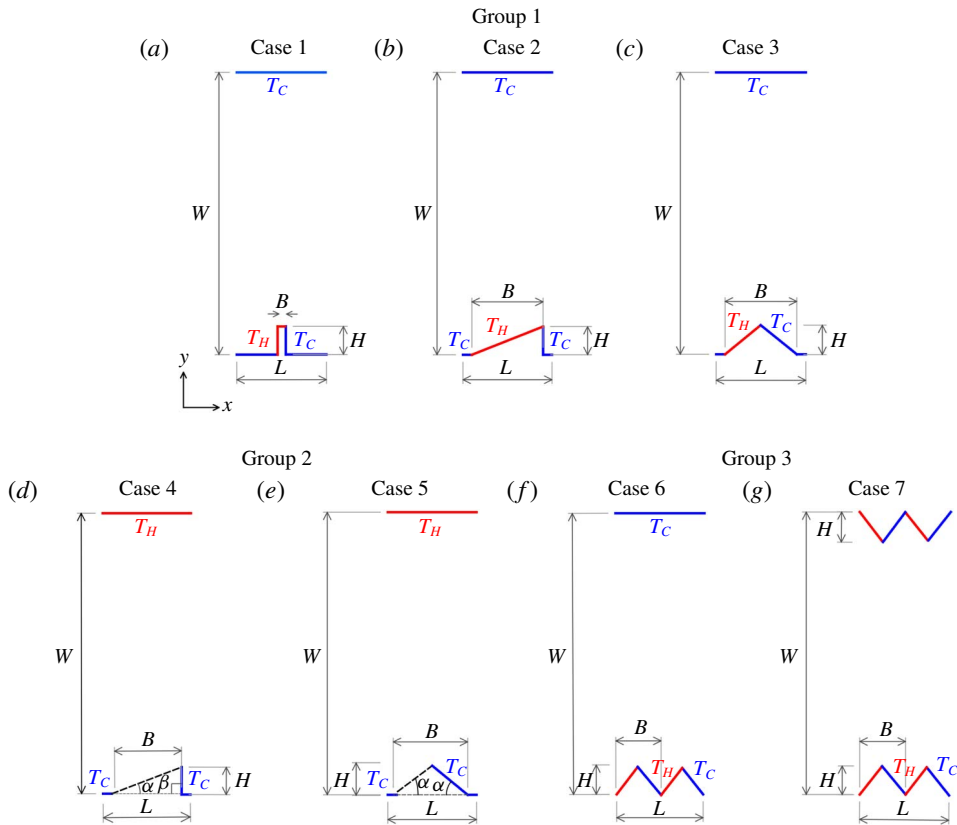
FIGURE 1. (Colour online) Schematic of the seven channel configurations categorized into three groups.

3. Problems

We considered nitrogen gas ($m = 46.5 \times 10^{-27}$ kg, $d = 4.17 \times 10^{-10}$ m) with a rotational relaxation collision number of 5 and a viscosity–temperature index of $\omega = 0.74$ at $T_{ref} = 273$ K. A two-dimensional simulation is assumed. The gas flows through the channels whose geometries are shown in figure 1. Seven configurations categorized into three groups are assessed for radiometric pumps.

The first group considers three variants of the Crookes radiometer. Case 1 represents a channel with an impeller of a standard Crookes radiometer on the bottom wall. Cases 2 and 3 are radiometric pumps with either a right-angled or isosceles triangle replacing the vane. Group 2 considers radiometric pumps utilizing vanes with one specular side, that is fins of cases 2–3 are utilized, but their left side was set as a specular reflector, as indicated by the dashed lines in the figure. Group 3 considers radiometric pumps with variants of double triangular vanes, e.g. in case 6, each triangle has half of the ratchet baseline shown in case 3, and, case 7 augments the same double ratchet pattern on the top wall, for instance, a zigzag channel. The case is analogous to applying the ratchets in case 6 to the half-domain.

The periodic boundary condition is implemented on both sides of the simulation domain. The vertical vane or slanted side wall(s) structure (right-angled or isosceles triangle) are of period L with a height H and baseline width of B. The sawtooth

Case	B/W	Side angles	$Kn = \lambda/H$
1	0.0095/4	$\alpha = 90°$	1
2, 4	1/4	$\alpha = 21.8°, \ \beta = 90°$	0.96
3, 5	1/4	$\alpha = 38.65°$	0.96
6, 7	0.625/4	$\alpha = 52°$	0.95, 0.90

TABLE 1. Geometrical specifications and set-up (for all cases $Kn = \lambda/W_{eff} = 0.1$).

geometries have ratios of $L/W = 5/16$ and $H/W = 0.1$ for all cases. The $H/W = 0.1$ ratio was recommended as the optimum tooth height for the maximum induced velocity and radiometric force (Shahabi *et al.* 2017). The specified periodicity ratio of $L/W = 5/16$ was suggested for the test case 4 in Shahabi *et al.* (2017); moreover, the results presented in Shahabi *et al.* (2017) showed that changes in the normalized periodicity length have small effects on the performance of case 4.

The temperature of the horizontal surfaces on the bottom wall is fixed at T_C, and a temperature ratio of $T_H/T_C = 2$ is considered between the hot (red lines) and cold (blue lines in figure 1) walls. The effect of changing the temperature ratio is investigated in §4.7. As the temperature cannot be set on the specular wall, the temperature difference is applied perpendicular to the channel axis. Thus, the upper boundary is considered as the hot wall in cases 4–5. For the other occasions, the left side of the vane/ratchet is set at a hot temperature, whereas the top wall is considered at T_C. Other geometrical specifications of the cases, including left and right side inclination angles, α and β, are reported in table 1.

If Kn is defined as the ratio of the gas mean free path and the characteristic length scale of the pump, and the latter is chosen as the effective height of the channel configuration, all cases, excluding those reported in §4.7 and the appendices, will have a $Kn = 0.1$. On this occasion, the effective channel height is defined as $W_{eff} = W - A/L$, where A/L represents the equivalent height of the vane or triangles, and $A = HB$ in cases 1 and 6, $A = HB/2$ in cases 2–5 and $A = 2HB$ in case 7. If we redefine Kn according to the height of the vane or ratchet, H, the simulated cases have a Kn ranging between 0.9 and 1, see the last column in table 1.

In the following, we report the normalized velocity and temperature as follows:

$$\hat{U} = \frac{|U|}{\sqrt{2RT_{avg}}}, \quad |U| = \sqrt{U_x^2 + U_y^2}, \quad T_{avg} = \frac{T_C + T_H}{2}, \quad \hat{p} = \frac{p}{p_0}, \quad \hat{\rho} = \frac{\rho}{\rho_0}, \quad \hat{T} = \frac{T}{T_C},$$
$$(3.1a-f)$$

where $\sqrt{2RT_{avg}}$ is the most probable velocity, U_{mp}, at the average temperature. p_0 and ρ_0 are the initial pressure and density, respectively.

4. Results and discussion

4.1. *Validation of the DUGKS solutions*

At this stage, two cases, 1 and 7, were simulated with the DUGKS solver and compared with the DSMC solutions for validation purposes of DUGKS simulations. Shown in figures 2 and 3 are the normalized velocity, temperature and density distributions over a vertical line connecting the tip of the vane/ratchet to the top wall/tip of the ratchet in cases 1 and 7, respectively. Frames in both figures depict suitable agreement between the DSMC and DUGKS solutions for both cases.
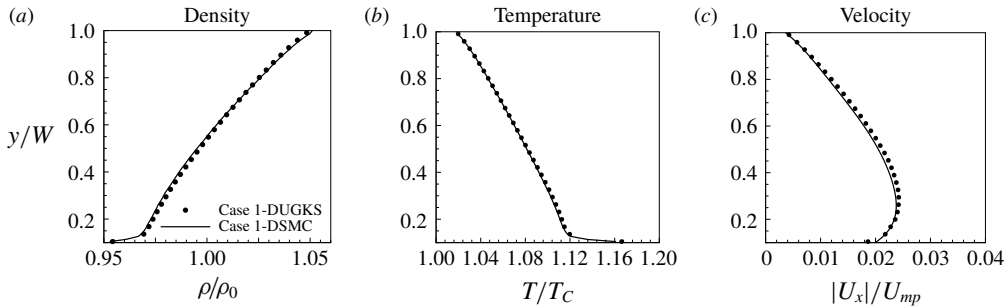
FIGURE 2. Comparison of DSMC and DUGKS solutions for flow field properties over a vertical line connecting the tip of the vane and the top wall, case 1.
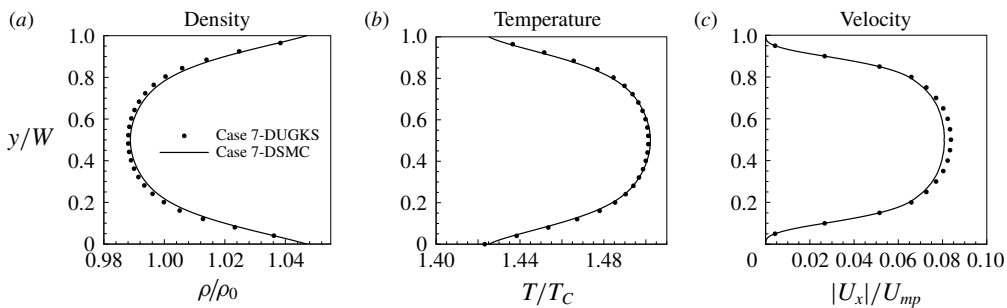

FIGURE 3. Comparison of DSMC and DUGKS solutions for flow field properties over a vertical line connecting the bottom and top tips at $x/W = 0.15625$, case 7.

Case	Solver	p_{avg} (10^{-2} atm)	ρ_{avg} (10^{-7} kg m^{-3})	T_{avg} (K)	$|U_{x_{avg}}|$ (m s^{-1})
1	DSMC	1.451	1.506	325.191	7.995
	DUGKS	1.451	1.505	325.297	8.428
7	DSMC	2.209	1.672	445.591	32.638
	DUGKS	2.193	1.656	446.499	33.415

TABLE 2. Comparison of flow field properties from DSMC and DUGKS.

A more detailed comparison is reported in table 2, where average temperature, density and velocity are compared between the solvers. Note that there are slight differences between the DUGKS and DSMC solutions at the investigated Knudsen number, $Kn \approx 1$. This is in agreement with the results reported in Zhu & Guo (2017a) at the transition regime, although such a difference was not observed at lower or higher Knudsen numbers. The slight discrepancy is attributed to the different treatments of the collision term between the Shakhov model used in the DUGKS and the VHS collision model employed in the DSMC simulations. It is expected that the effect of the different treatments of the collision term of the Boltzmann equation is more significant in the transition regime compared to other flow regimes (Zhu & Guo 2017a).
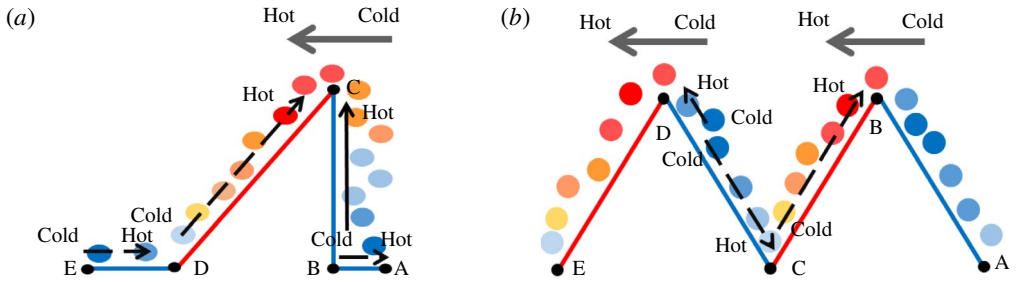
FIGURE 4. (Colour online) Schematic of flow mechanism in (*a*) cases 2 and (*b*) 6–7, circular symbols depict gas particles, and their colours depict gas temperature.

4.2. *Mechanism of the flow*

The flow mechanism is almost similar in all configurations considered in this study. Because of the temperature field, there is a radiometric force in the positive axial direction near the tips of the vane/ratchet. The reaction of this force in the negative direction is transferred to the gas near the edge as momentum transfer. This transmission of momentum to the gas is caused by molecular collisions between the reflected molecules and the neighbouring molecules. At the investigated *Kn*, that is $Kn \approx 1$, this transmission takes place within a region extending one mean free path above the tip; thus, the flow becomes stronger in this region almost independently of the geometry.

As figure 4 schematically depicts, temperature gradients around the structure's tip and on the bottom left horizontal surface, or on the inclined cold surfaces in cases 2–3 and 6–7, drive the flow in two opposing directions. Although the temperature of the bottom left wall (cases 1–5) or inclined cold surfaces (cases 1–3, 6–7) is constant in all of the cases, as will be shown in the sequel to this paper, a gas temperature gradient arises along the boundaries; thus, producing a rightward (or leftward in cases 6–7 over the inclined cold wall near the tip) thermally driven flow over them, as indicated by the arrows with dashed line. The nature of this rightward (or leftward) flow resembles thermal creep flow, and hereby, we call it 'rightward (or leftward) flow induced with the same mechanism as thermal creep flow' or simply 'rightward (or leftward) flow'. Indeed, the rightward flow seems to be weaker than the radiometric flow at the tip, and the rightward flow is blocked by the vertical/inclined left wall. (Note that the ratio of the rightward flow to the radiometric flow varies from case to case, and changes in strength at lower *Kn*, see appendix C.) At the investigated *Kn*, the net flow is directed leftward by the abrupt temperature shifts around the tip(s), and is therefore, against the rightward flow on the left horizontal or inclined walls.

4.3. *Velocity and temperature fields*

Figure 5 reports the isolines of the normalized velocity contours and streamlines for all of the cases. To distinguish between the cases, the maximum velocity scale is the same for all panels in figure 2. The actual maximum for each case is reported in table 3. Figure 6 shows close-up views of velocity isolines and streamlines around the tip of the vane/ratchets.

Figures 7 and 8 depict normalized velocity profiles over a vertical line connecting the tip of the vane/tooth on the bottom wall to the top wall (cases 1–6) or to the ratchet tip on the top wall (case 7) and over a cross-section connecting the left
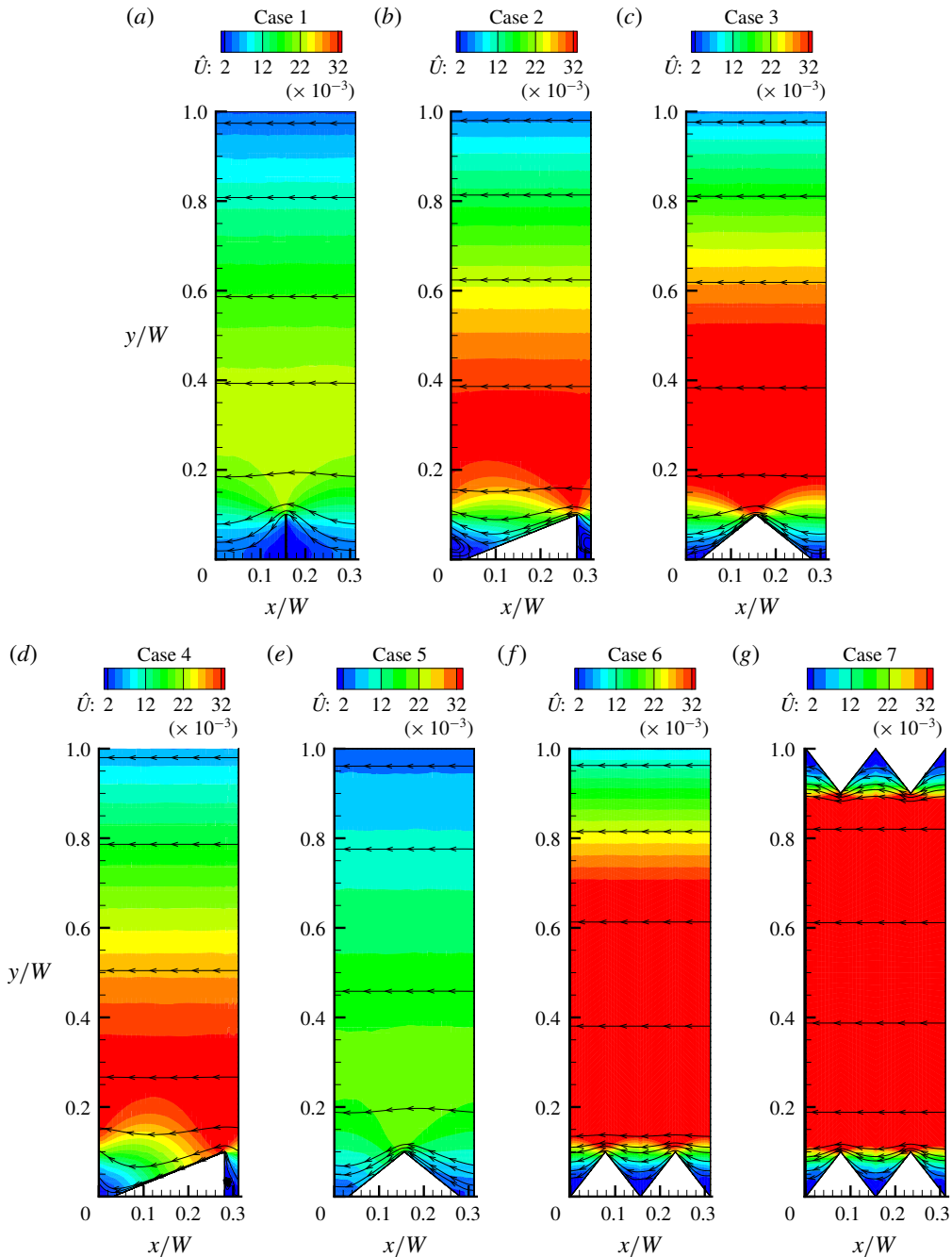
FIGURE 5. (Colour online) Isolines of the normalized velocity magnitude and streamlines, DSMC solutions.

troughs (cases 1–5) or middle troughs (cases 6 and 7) on the bottom wall to the top wall, respectively. Even though the height of the vane and ratchets is the same in all the cases, the results shown in figure 5 clearly indicate that the design using the conventional radiometer impeller (case 1 in group 1) is less efficient compared to
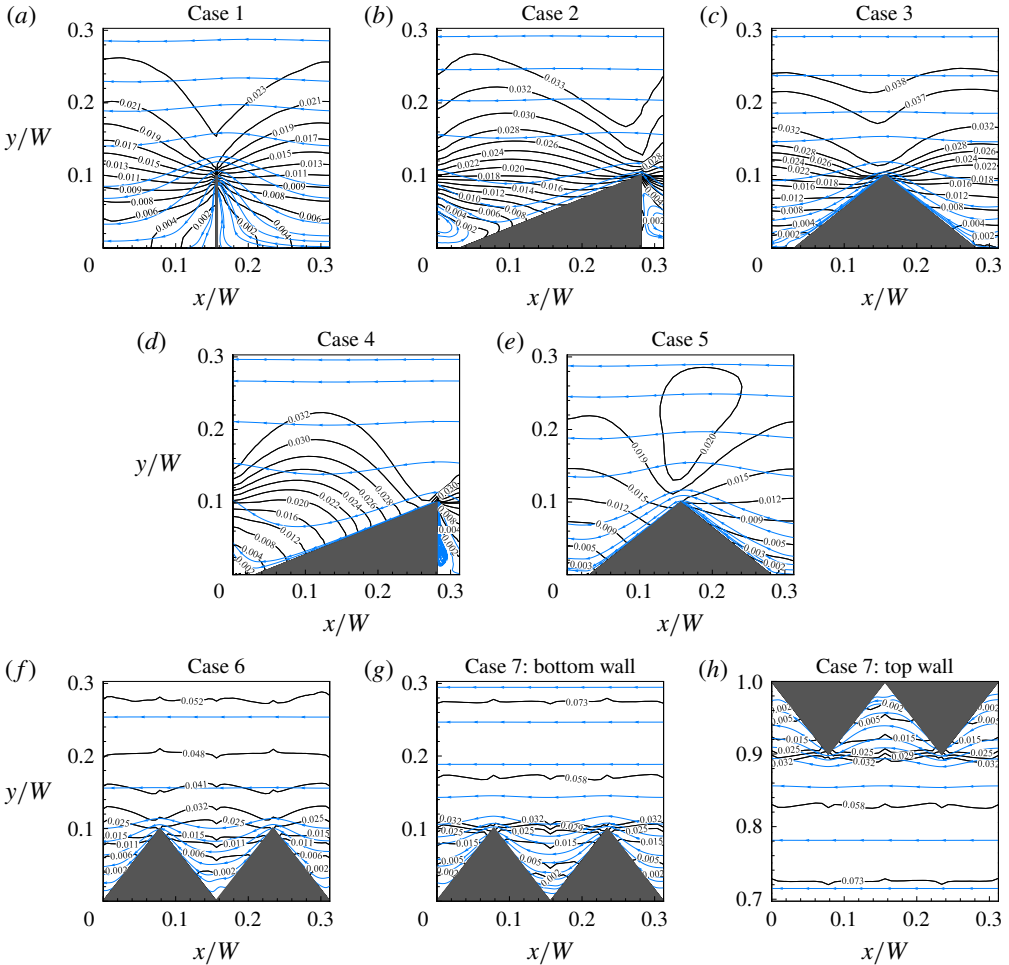
FIGURE 6. (Colour online) Close-up view of normalized velocity isolines and velocity streamlines around the tips of the vane/ratchet, DSMC solutions.

most of the ratchet pumps in terms of induced velocity. In addition, the shape and arrangement of the teeth strongly influence the induced velocity. The performance of the cases in group 1 improves from case 1 to 3, that is the induced velocity increases, and maximum velocity occurs for isosceles triangular fin, see figures 5(*a–c*), 7(*a*) and 8(*a*). However, in the second group, figures 5(*d–e*), 7(*b*) and 8(*b*), where the left inclined surface is specular, the induced velocity is higher for a right-angled triangle. As will be discussed later, the reason behind this difference lies in the produced discontinuity in the temperature field under these two conditions. The panels (*f−g*) in figure 5 and panel (*c*) in figures 7 and 8 show that case 7 outperforms case 6 in the third group. Figure 6(*b*) shows the formation of a vortex near the junction of left horizontal to left inclined surface and right vertical wall and its adjacent horizontal walls. Figure 6(*d*) depicts a small vortex adjacent to the right vertical wall of the ratchet.

According to figures 7 and 8, in all of the cases except for case 7, the velocity field in the open channel is similar to Couette flow, that is, the velocity decreases
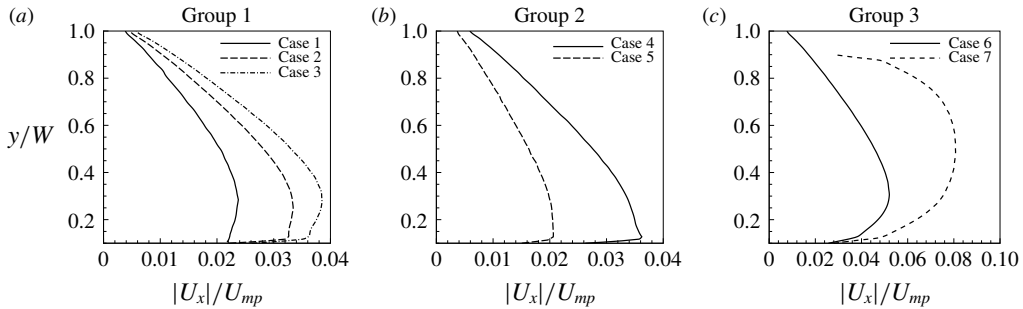
FIGURE 7. Velocity distribution over a vertical line connecting the tip of the vane/tooth and the top wall (cases 1–6) and ratchet tip (case 7), DSMC solutions.
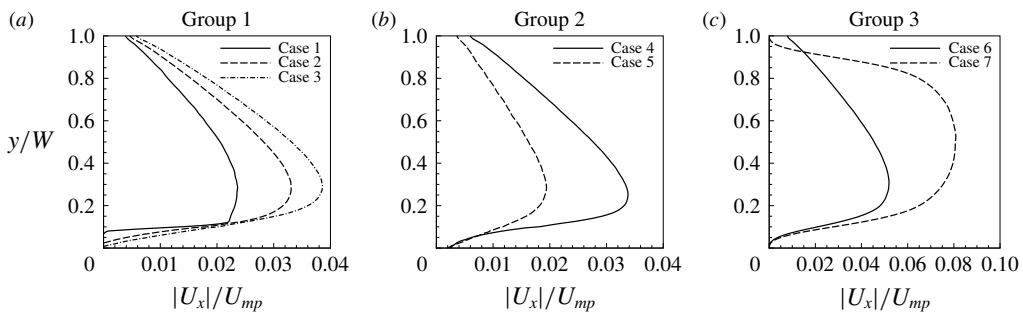

FIGURE 8. Velocity distribution over a vertical line connecting the bottom left vertex of the vane/tooth (cases 1–5) or middle troughs (cases 6–7) to the top wall, DSMC solutions.

almost linearly from a few mean free paths above the vane/ratchet tip towards the top wall. On these occasions, the vane/ratchet tip acts as a localized force source in its vicinity. Due to momentum conservation, the reaction of the radiometric force is on the top wall but of shear origin in the negative direction, for instance, τ_{12}. Thus, the velocity approximately scales as $\tau_{12}(W-H)/\mu$ for low Kn flow above the ratchet/vane (Shahabi *et al.* 2017).

Nevertheless, the velocity profile in case 7 is parabolic-like in both figures 7(*c*) and 8(*c*). The quadratic profiles in case 7 are a consequence of the radiometric flow above the tips retarded by the strong frictional drag force of the ridges and the opposite flow mechanism at the troughs. However, the rightward induced flow at the trough is blocked by the inclined wall and confined inside the triangular region formed by the two tips and the trough. Due to the large mean free path of the gas, for instance, $\lambda \sim H$, flow is actively caused in the region approximately one mean free path away from the tips above them (Taguchi & Aoki 2012). This flow is retarded by the friction of the zigzag surfaces on both the bottom and top walls, thus, the flow velocity takes a parabolic profile with small magnitude near the walls. The velocity profile bears a resemblance to the thermal transpiration between two horizontal plates (Ohwada, Sone & Aoki 1989; Takata & Funagane 2013).

Figure 9 shows the temperature jump distribution over vertical or inclined lines passing the surfaces of the bottom wall. The horizontal axis in the figure is indicated by s, and is normalized by the channel height. The abbreviations in the figure stand for the wall orientation (e.g. HL: horizontal left, VL: vertical left, IL: inclined left, HR:
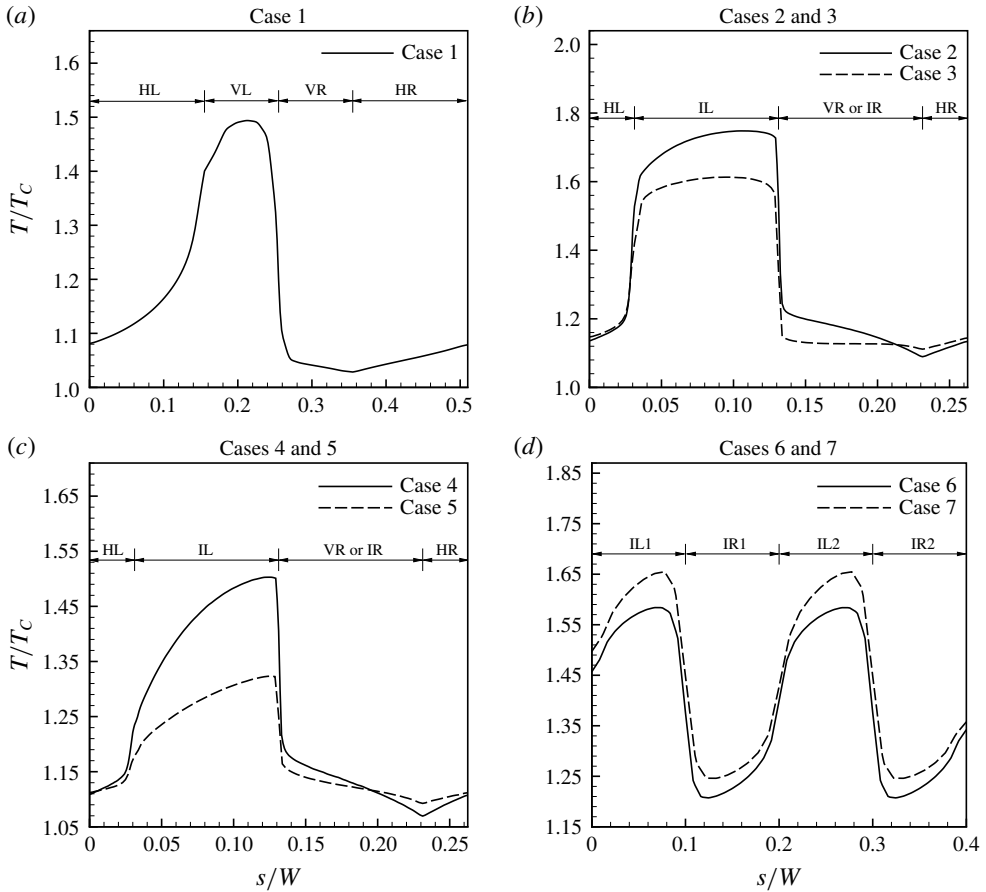
FIGURE 9. Temperature jump distributions on the bottom surfaces, DSMC solutions.

horizontal right, VR: vertical right, IR: inclined right). Comparison of the temperature profiles with the velocity fields, shown in figures 7 and 8, indicates that velocity is influenced by the magnitude and the number of discontinuities in the temperature profile together with surface resistance (drag force).

The profile of case 1 shows a gradual increase in $0 < s/W < 0.22$ and a sharp decrease at $s/W = 0.25$. The former corresponds to temperature elevation on the left horizontal wall and the vertical left wall, and the latter is related to the temperature difference between the hot side and the cold side of the vane. Evidently, the temperature gradient is larger around the vane's tip, and the frictional retarding effect is present against the rightward flow.

Compared to case 1, cases 2 and 3 show two jumps in the temperature profiles at junctions of the left horizontal and the left inclined hot surface and the left inclined hot wall and its adjacent cold wall. A symmetrical geometry, case 3, produces almost a symmetrical temperature profile at its surrounding, but the right-angled fin used in case 2 produces a stronger temperature gradient at the left horizontal-inclined wall junction, while its resulting temperature gradient at the tip is almost the same as that in case 3. In conclusion, a net leftward induced flow is reduced in case 2 compared to case 3. The formation of a vortex near the junction, as shown in figure 6(*b*), is

Group	Case	$\hat{U}_{max}$	$\|U_{x_{max}}\|$ (m s^{-1})	$\|U_{x_{avg}}\|$ (m s^{-1})
	1	0.024	12	7.995
1	2	0.034	17	11.580
	3	0.039	18	13.474
2	4	0.036	18	11.751
	5	0.021	10	6.925
3	6	0.052	26	18.115
	7	0.081	40	32.638

TABLE 3. Maximum and average velocity in cases 1–7, DSMC solutions.

also the consequence of stronger rightward flow in case 2. As a conclusion, where both ratchet walls are diffuse reflectors, reducing the length of the left inclined wall from case 2 to 3 is in favour of inducing a higher fluid velocity.

If we turn to cases 4 and 5, a similar phenomenon is observed, that is, a right-angled triangle produces a stronger temperature discontinuity on the left horizontal-inclined wall junction, but on this occasion, the induced temperature gradient at the tip is also much sharper in case 4. This is the reason for a higher induced velocity in case 4 compared to case 5. As the resistive force on the inclined left surface is removed due to its specular nature, the rightward flow tends to move up the left inclination in case 5, but it is blocked at the leftward tip flow.

Temperature jumps on bottom walls in cases 6 and 7, plotted in figure 9(*d*), depict four discontinuities. As depicted in figure 4(*b*), the temperature jump in most parts of the troughs induces a rightward flow towards the tip. The discontinuities near the tip induce a leftward flow; thus, two flows of opposite direction are induced. The leftward flow is stronger due to a sharper tip temperature gradient, and as previously noted, wall friction retards (slows down) the rightward flow. Note that the strength of the temperature gradient is almost the same in both cases, but the advantage of case 7 is that the same acceleration mechanism exists on the top wall.

Table 3 summarizes the maximum and average velocities in each case. Considering figures 5–8 and table 3, it is concluded that case 5, patterned with an isosceles triangle with one specular side, is the least efficient design followed by the design inspired by the conventional radiometer, e.g. case 1. On the other hand, cases 6 and 7 show extremal velocity fields, respectively. The use of double triangles on both walls of the pump boosts the velocity field by almost 1.8 times compared to case 6. However, there is no practical benefit if the specular side of a right-angled triangle changes to a diffusive wall (compare cases 4 and 2). It should be remembered that cases 6 and 7 have a higher heat flux input, with two and four side walls with a temperature discontinuity, respectively, compared to the previous cases. This argument will be discussed when considering the thermal efficiency of the cases.

Shown in figure 10 are the close-up views of the normalized temperature contours around the edges of the vane/ratchets for all of the investigated cases.

For almost all of the cases, apart from case 7, temperature isolines above $y/W = 0.3$, not shown here, are reasonably parallel to the upper wall with a constant spacing between the isolines. Cases 4, 5 and 7 experience a higher temperature inside the domain as the top wall or some of its segments are set at T_H. Temperature patterns at the tip entirely differ from one case to another; for instance, in case 1, isolines
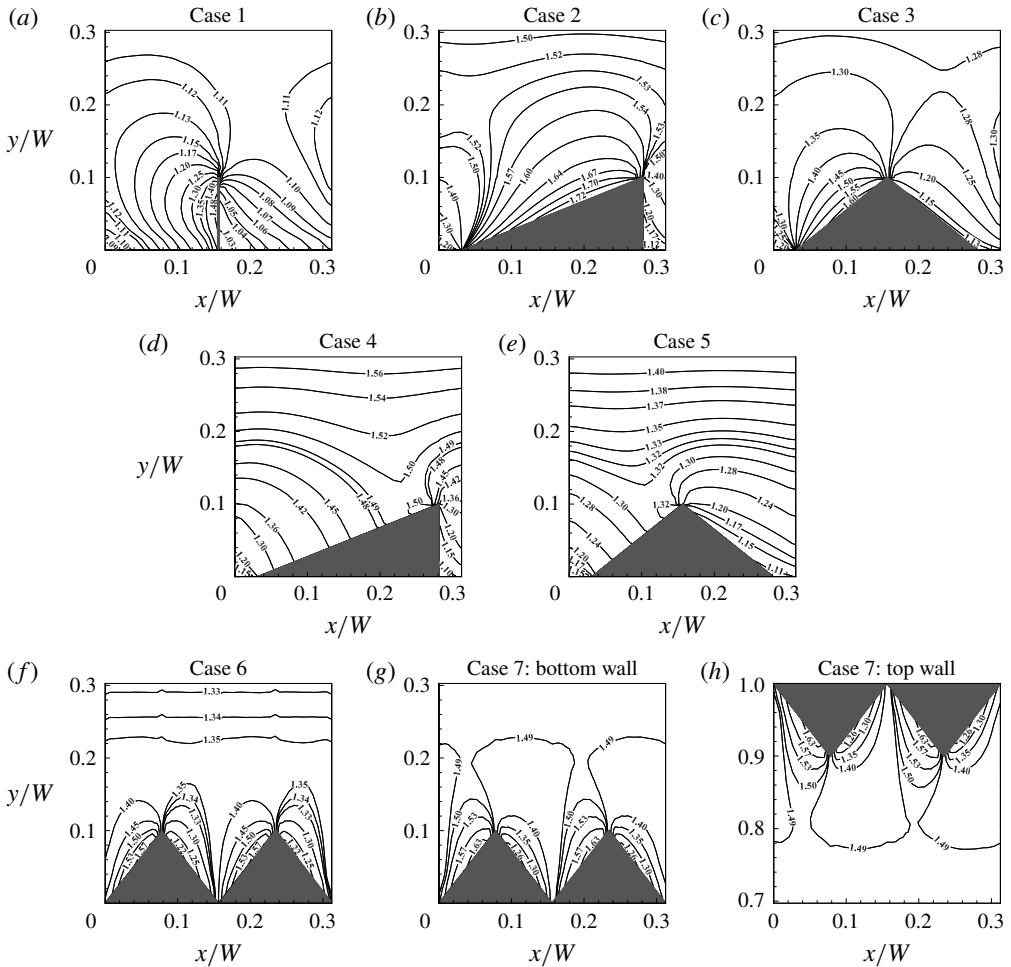
FIGURE 10. Isolines of normalized temperature around the tip of the vane/ratchet, DSMC solutions.

originate from the tip asymmetrically and are immersed on the left horizontal wall. The slope of isotherms increases and they become condensed as they approach the impeller from the left side. A notable difference between diffuse–diffuse conditions (cases 2–3 in group 1) and specular–diffuse cases (cases 4–5 in group 2) is the accumulation of the isolines at the bottom left vertex of the tooth in the former cases, while in the latter cases, most isolines become perpendicular on the specular side. Case 3 shows that the temperature isolines are almost asymmetric, T increases above the cold side on the right, while it decreases above the hot side on the left. The degree of asymmetry, that is the distance between two isolines with the same magnitude, is stronger compared to that in case 5 with a specular side on its left. On all occasions, the isolines concentrate at the tip of the geometry. Thus, the macroscopic temperature is singular there.

In cases 4–5, isotherms starting from slightly left of the tip and the tip itself land almost normally on the specular surface. This behaviour arises from the adiabatic nature of specular walls. Lower value isolines start from the right surface and
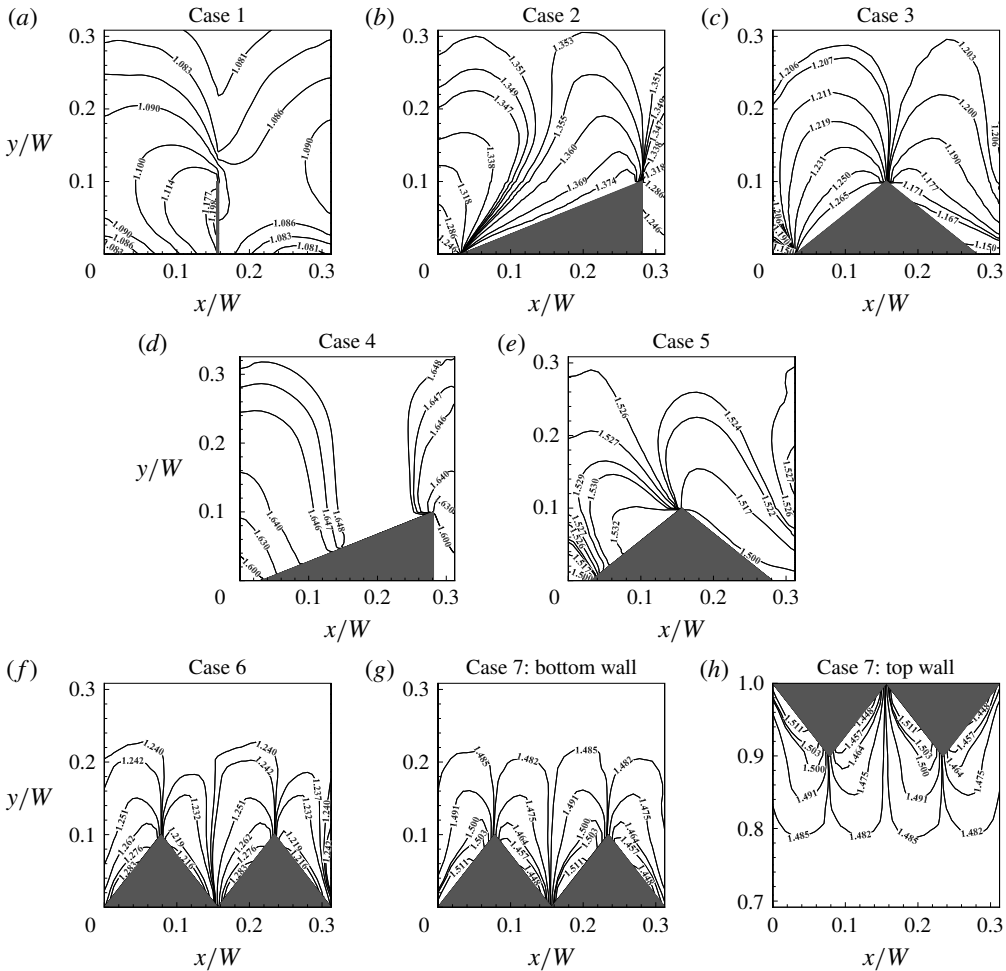
FIGURE 11. Isolines of the normalized pressure around the tip of the vane/ratchet, DSMC solutions.

accumulate on the bottom left vertex of the triangle. The vicinity of the tip and bottom left vertex are where the thermal stresses become extremal. The comparison of cases 6 and 7 indicate that double triangular fins on both top and bottom walls act similar to those in case 6 but with a steeper temperature jump on both sides of the teeth in case 7. In this condition, each set of ratchets influences one half of the domain, producing a symmetrical temperature field with respect to the channel centreline.

4.4. *Pressure distribution*

Figure 11 demonstrates normalized isobars for the simulated cases. In all of the cases, the pressure distribution is uniform far from the ratchet/vane tip within the open section of the geometry.

In case 1, the pressure field is almost homogenous on the right side of the vane, while it rapidly changes on its left side where the temperature is high and

inhomogeneous. This is the effect of thermalized molecules leaving the hot side of the plate and populate in its vicinity (Taguchi & Aoki 2012). In cases 2–3 and cases 6–7, the starting point and destination of most isobars are the ratchet tip and its left vertex, respectively, indicating the presence of steep pressure gradients at the tip and in the vicinity of the left vertex of the ratchet in the case of diffusive left inclined sides. Considering case 4 in group 2, the upper half of the inclined side experiences a constant pressure while the isobaric lines departing from the tip and its vicinity curve back onto the lower half of the specular surface. Case 5 presents a smaller pressure difference between the ratchet sides, and isolines end at the bottom half of the inclined side and accumulate near the bottom left vertex. Both ratchets in case 6 experience the same pressure difference on their sides. Even though the pressure difference on both sides of each ratchet is smaller than that in case 3, the increase in the active area where this pressure difference is applied makes case 6 more efficient in terms of induced velocity. Case 7 experiences higher pressure magnitudes around the fins compared to case 6. This corresponds to a higher temperature gradient occurring around the fins in the latter case.

4.5. *Radiometric force*

Here, we compute the radiometric force on the configurations considered in the previous sections. For all of the considered geometries, the resultant force in the axial direction induces a net flow from right to left. In DSMC, the force density exerted on a solid wall f_D is computed as the momentum change between the incident and the reflected streams:

$$f_D = \frac{N_{equ}}{\delta t \, dA} \sum_{j=1}^{N_s} m(\xi_j^r - \xi_j^i), \tag{4.1}$$

where N_{equ} is the number of real molecules represented by a DSMC particle, dA is the wall surface element and summation is computed over all N_s particles interacting with the surface element. Superscripts r and i refer to incident and reflected particles, respectively. The net force on the geometry is computed by integrating the force density over all surfaces at the top or bottom of the geometry. Note that horizontal side walls adjacent to the ratchet/vane also contribute to the axial force.

To explore the axial radiometric force, the normalized axial force ($f_{D,x}/p_0$) distribution on vertical and horizontal walls on the bottom surface are plotted in figure 12(*a–g*) for all of the cases. Figure 12(*a,c,e,g*) indicates that the axial force is almost positive except in the upper half of the ratchets in case 7, but the force on the horizontal surfaces, figure 12(*b,d,f*), is negative, confirming the tendency of the flow to move rightward there. This is the essential difference between the force mechanism here and in the standard Crookes radiometer or its typical variants considered in the literature (Selden *et al.* 2009; Ketsdever *et al.* 2012; Taguchi & Aoki 2012, 2015; Baier *et al.* 2017). The vanes of the standard radiometer are usually far from the chamber walls and the force mechanism exists only around the vane. Here, the temperature discontinuities on the bottom left horizontal wall of the channel (cases 1–5) and inclined walls of the ratchet (cases 6 and 7) directly influence and reduce the net positive force. Therefore, the distribution of the local force here cannot be interpreted via the radiometric force only.

In case 1, there is a significant temperature gradient along the bottom left wall, see figure 9(*a*). This temperature gradient causes a flow driven by the same mechanism

(*a*) Case 1: on the vane

(*b*) Case 1: over the horizontal walls

(*c*) Cases 2 and 3: on the ratchet

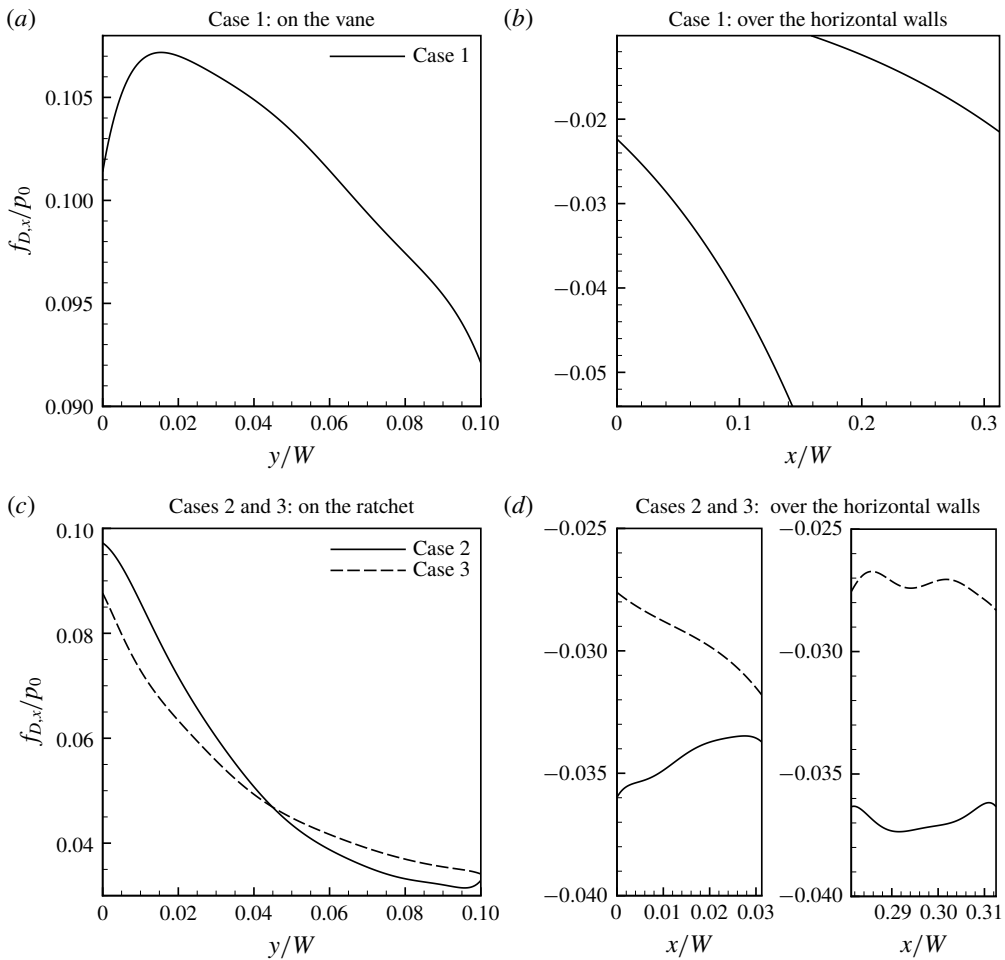(*d*) Cases 2 and 3: over the horizontal walls

FIGURE 12. For caption see next page.

as thermal creep in the positive axial direction, and in reaction, a shear stress in the negative axial direction is exerted on the wall. This accounts for the sharp negative stress for $x/W < 0.15$ in figure 12(*b*). Along the vane, figure 12(*a*), there is a rise and a fall in the force towards the tip. The rightward flow in the positive direction on the horizontal left wall is blocked by the vane and pushes it; the rise in force around $y/W \approx 0.01$ is due to this pushing effect. As soon as the pushing effect disappears, the so-called area force, that is, the molecular momentum difference between the hot and cold sides, prevails. However, the force is smaller near the tip compared to the middle parts of the vane.

In figure 12(*d,f*), the shear stress is almost negative. However, the length of the bottom horizontal walls on both sides of the ratchet is much smaller in cases 2–5 compared to case 1. The radiometric force distribution, plotted in figure 12(*c,e*), shows a different pattern from radiometric flow over the vane of a Crookes radiometer. For cases 2–4, the peak in force is shifted toward the root of the ratchet, and the force magnitude decreases towards the tip. The force pattern in case 4 is similar to case 1, while in case 5 the ratchet area produces a radiometric force with limited variations. Note that case 4 possesses a lengthier specular side and a more asymmetric shape
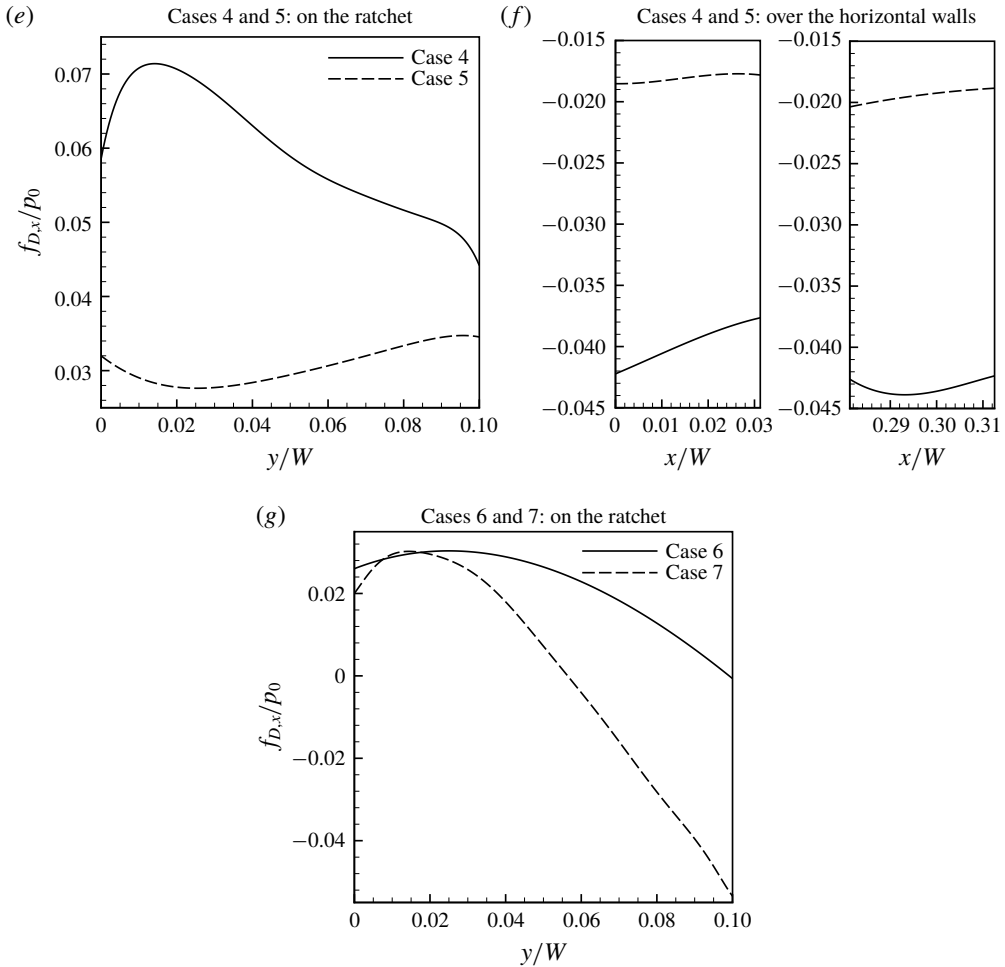
FIGURE 12 (cntd). Force distribution on (*a,c,e,g*) vane/ratchet, (*b,d,f*) horizontal bottom surfaces, DSMC solutions.

compared to case 5, hence, a stronger temperature gradient, as plotted in figure 9(*c*), and radiometric force is envisaged. Nonetheless, the larger variations of temperature in case 4 result in stronger rightward flow, and thus, a negative shear stress on the horizontal wall compared to case 5.

Force distributions in cases 6 and 7 plotted in figure 12(*g*) depicts an increasing–decreasing trend. Note that the force distribution is identical on each ratchet in cases 6–7. The force magnitude is positive in case 6 with a non-zero net force, while the force in case 7 is negative for $y/W > 0.55$ regions near the tip of the ratchet. In all the cases excluding case 7, there are horizontal surfaces on the top wall of the channel where the reaction of the radiometric force is transmitted through the gas, and the total force acting on the vane/ratchet plus all the horizontal walls is zero. Nonetheless, in case 7, all the momentum is transmitted to the gas. If this momentum is not zero, the gas is accelerated or decelerated. In the steady state, therefore, the force acts on the zigzag walls, and thus, the momentum transmitted to the gas, should be zero. This is indeed the situation encountered in the thermal creep problem, where shear stress

is absent over the walls at steady state conditions (Takata & Funagane 2013). The resemblance of the force condition supports our previous argument on the similarity of the velocity profile of case 7 to thermal creep between two horizontal surfaces.

Table 4 reports the axial and normal force per wall and the total force for all of the cases. Apart from case 1, the negative contributions of the horizontal left and right bottom walls to the axial force are much smaller than the positive contribution of the vertical/inclined sides of the ratchet, that is, $O(10^{-5})$ versus $O(10^{-3})$. In the first group, the maximum force on both sides of the ratchet occurs in case 2, but the net force, and thus the induced velocity, are smaller than those in case 3. The higher force on the sides of case 2 is in agreement with the observed higher temperature on both sides of the ratchet as shown in figure 10(b). In the second group, the axial force on the ratchet sides and the net force is greater in case 4 than in case 5, which is again in agreement with the higher gas temperature reported in figure 10(d) compared to figure 10(e). Even though the temperature, and hence the velocity, of impinging particles around the specular sides of the fins of both cases in group 2 is lower than in cases 2 and 3, the force on both sides of cases 4 and 5 is maximum among the first six cases. The reason seems to be a higher number of particles (N_s) impinging and transferring momentum with the surfaces in both cases in group 2 due to a greater gas density around the ratchets with one specular side. For example, the gas density is larger by approximately 41 % on the inclined surface and by 33 % on the vertical surface in case 5 compared to the corresponding value in case 3. The net axial force, however, is small in case 5 due to a limited temperature asymmetry around the ratchet.

The axial force of case 4 is maximal among the first and second group cases. Referring to table 3, this maximum force is approximately accompanied with the maximum induced velocity around the tip but not with the maximum average flow velocity among the first five cases. Again, a lower flow average velocity in case 4 in comparison with case 3 could be attributed to its higher average density; thus, the net force in case 3 accelerates the gas particles more. On the other hand, the maximum force in all cases occurs in case 6. Case 7, with a zero net force, experiences a relatively large axial force over each wall, but in opposite directions for each adjacent surface. Mind that each pair of ratchets accelerates the half-domain in case 7.

4.6. *Mass flux and efficiency*

Table 5 summarizes the field properties and normalized mass flux in all of the cases. Both cases in group 2 have a higher average temperature and pressure compared to all other cases. They are followed by case 7. The average VHS mean free path at steady state is approximately the same for all cases, except for cases 1 and 7. This is in agreement with the equality of the initial Knudsen number, based on the equivalent channel height, of the cases enforced at the beginning of simulations.

Normalized mass flux is calculated over a vertical line connecting the bottom surface to the top one, that is:

$$\hat{j} = \frac{\displaystyle\int_0^W \rho U_x \, \mathrm{d}y}{\rho_0 \sqrt{2RT_C} W}.$$ (4.2)

Case 7 is the optimum design in terms of maximum mass flux due to its higher induced velocity.

Group	Case	Horizontal left wall		Vertical or inclined left wall		Vertical or inclined right wall		Horizontal right wall			
		F_x (10^{-5})	F_y (10^{-3})	F_x (10^{-3})	F_y (10^{-2})	F_x (10^{-3})	F_y	F_x (10^{-5})	F_y (10^{-3})	F_x (10^{-4})	F_x/F_y (10^{-3})
1	1	−31.20	−8.91	6.47	−0.003	−5.93	-4.61×10^{-5}	−12.6	−8.88	1.06	−5.89
	2	−6.00	−2.08	7.37	−1.93	−7.08	-9.19×10^{-5}	−6.43	−2.08	1.65	−6.99
	3	−5.14	−1.95	7.03	−0.90	−6.75	-8.05×10^{-3}	−4.76	−1.96	1.81	−8.64
2	4	−6.94	−2.73	9.26	−2.31	−8.93	-1.73×10^{-4}	−7.55	−2.73	1.87	−6.50
	5	−3.16	−2.61	8.63	−1.08	−8.46	-1.06×10^{-2}	−3.40	−2.62	1.05	−3.97

Group	Case	Inclined left wall-1		Inclined right wall-1		Inclined left wall-2		Inclined right wall-2			
		F_x (10^{-3})	F_y (10^{-3})	F_x (10^{-3})	F_y (10^{-3})	F_x (10^{-3})	F_y (10^{-3})	F_x (10^{-3})	F_y (10^{-3})	F_x (10^{-4})	F_x/F_y (10^{-3})
3	6	7.15	−5.75	−7.02	−5.15	7.15	−5.75	−7.02	−5.15	2.56	−11.76
	7	8.83	−7.20	−8.83	−6.61	8.83	−7.20	−8.83	−6.61	0	0

TABLE 4. Force per area on each wall, net force (N m^{-1}) and force ratio, DSMC solutions.

Group	Case	T_{avg} (K)	p_{avg} (10^{-2} atm)	λ_{ave} (10^{-1} m)	$\hat{j}$ (10^{-2})	q (J)	η (%)
	1	325.191	1.451	4.004	1.879	0.224	0.376
1	2	409.899	1.883	3.889	2.540	1.283	0.149
	3	362.690	1.678	3.861	3.006	0.684	0.358
2	4	498.761	2.302	3.871	2.718	1.204	0.182
	5	465.059	2.131	3.899	1.615	1.555	0.047
3	6	373.862	1.745	3.827	4.009	0.823	0.565
	7	445.591	2.209	3.604	6.985	0	—

TABLE 5. Flow field properties in all investigated cases, DSMC solutions.

The performance of cases 2 and 4 is quite comparable in terms of the induced mass flux in the field. Thus, case 4 is comparable with its geometrical counterpart in the first group in terms of induced mass flux even though its maximum velocity was close to that in case 3. The latter produces the maximum mass flux among all of the members of groups 1 and 2. Case 5, with an isosceles triangle, performs worst in inducing mass flux.

The overall efficiency of the simulated pumps considered as a model heat engine is defined as the ratio of the extracted power to the net heat flux along the bottom walls of the pump. Output power is estimated as the multiplication of the average field velocity and the axial radiometric force density on the bottom wall (i.e. $Po = F_x U_{x_{avg}}$). Accordingly, the efficiency is given as:

$$\eta = \frac{Po}{q}. \tag{4.3}$$

Among cases 1–6, maximum efficiency corresponds to case 6 due to the higher induced velocity compared to the lower bottom wall heat flux input, while minimum efficiency corresponds to case 5 because of the low induced velocity despite its high heat flux input. Heat flux input in case 7 is almost zero, that is, the heat flux provided by the hot wall is absorbed by its adjacent cold wall. In harmony with previously designed radiometric pumps, the efficiency of all the configurations is small, less than 1 % (Zhu & Guo 2017*b*).

4.7. *Mass flux dependence on wall temperature and Knudsen number*

Here, we use DUGKS to investigate the dependence of the pumping performance of two typical cases on the temperature difference and Knudsen numbers. The deterministic nature of the DUGKS makes it more competitive than the DSMC for cases with a small temperature difference or smaller Knudsen number. Shown in figure 13 is the mass flux dependence of cases 1 and 7 on the normalized temperature difference ($\Delta T/T_c$) of the adjacent walls. The difference between the hot and cold walls was increased from 50 K to 600 K. In case 1, mass flux increases between the adjacent temperature differences with the slope of the lines decreasing as the temperature difference increases. A similar decrease in line slope is observed in case 7.

The dependence of mass flux on ΔT is nonlinear in both cases except for small temperature differences, that is $\Delta T < 200$ K in case 1 and $\Delta T < 100$ K in case 7.
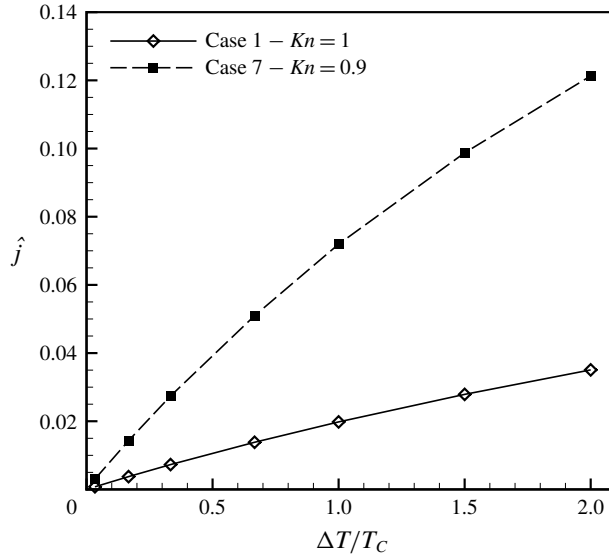
FIGURE 13. Normalized mass flux dependence on the wall temperature difference for cases 1 and 7, DUGKS solutions.

Even though the mass flux of cases 1 and 7 is close at the smallest ΔT, the difference between mass flux increases sharply with an increase in ΔT. Thus, the benefit of using case 7 is enhanced at higher wall temperature differences. Moreover, the deviation from a straight line is stronger in case 7.

Figure 14 depicts variations of the normalized mass flux with the Knudsen number for cases 1 and 7, where DUGKS and DSMC solutions are compared. Mass flux is reported at Knudsen numbers of 0.01, 0.1, 0.5, 0.9 (just in case 7), 1 (just in case 1), 2.5, 5 and 10. In agreement with our discussion in § 4.1, the difference between the mass flux predictions of DUGKS and DSMC is minor in small rarefaction regimes or $Kn > 1$, while the difference is sensible in the transition regime. More deviation between DSMC and DUGKS solutions are observed in case 7.

From $Kn = 0.01$ to $Kn = 0.5$, the mass flux increases almost 4.5 times in case 1 and around 10 times in case 7. Moreover, the mass flux in both cases increases with Kn up to a Knudsen number of 0.5 and decreases as Kn increases in the transition regime. The maximum mass flux, however, occurs at around $Kn \approx 0.5$ in both cases. Within the investigated range of Knudsen number, the mass flux variations could be approximated with $[a/Kn^{0.5} + bKn^{0.5}]^{-1}$ in case 1 and $[a/Kn^{0.6} + bKn^{0.6}]^{-1}$ in case 7, where a and b are two constants that differ from case to case. The difference between the least-squares fit exponent of both cases lies in their different temperature field structures.

5. Concluding remarks

The current work revisited radiometric channel pumps bounded by various configurations investigating the fluid physics, ratcheting pattern effects and further mechanical applications. DSMC method was successfully employed to analyse the flow and thermal fields, as well as the performance of a series of arrangements for radiometric channel pumps ranging from a simple model inspired by Crookes radiometer to sawtooth structures on both top and bottom walls of the channel. Here,
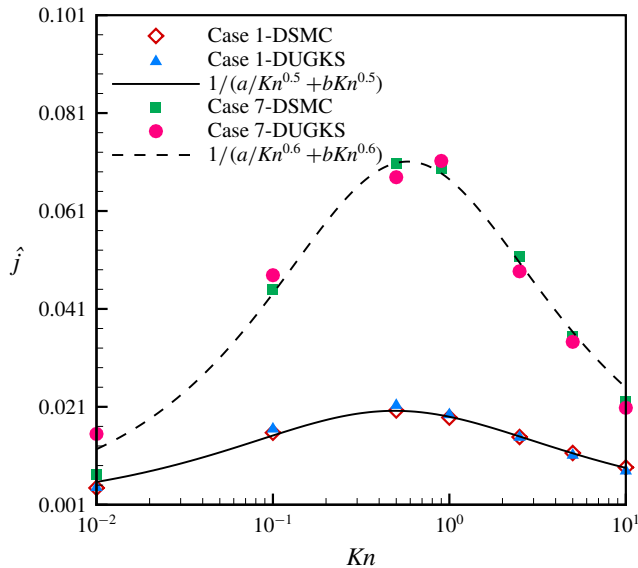
FIGURE 14. (Colour online) Dependence of the normalized mass flux on *Kn*, comparison of DSMC and DUGKS solutions.

it was suggested that diffusive walls be used but that the blade temperature be set differently to create an axial temperature gradient at the tips of the vane/tooth.

Most of the reported simulations were performed at $Kn \approx 1$, based on the impeller height. Thus, abrupt temperature variation near the edge extends roughly to a region one mean free path away from the edge. It was shown that the local mechanism that induces the flow works equally for all of the cases; therefore, the magnitude of the overall flow is determined by the strength and number of discontinuities in the resulting temperature profile near the tips, the resistance due to the geometry, the surface properties of boundaries and opposing rightward flow on the horizontal wall connected to the vane/ratchet or inclined plate.

We showed that the maximum radiometric force corresponds to a pump with double ratchets on the bottom wall, but maximum pumping velocity and mass flux are attained if a zigzag channel with teeth imposed on both the bottom and top walls is utilized. Radiometric force is produced due to the difference in particle momentum on both sides of the fins, and the force mechanism of the investigated cases clearly differed from the standard Crookes radiometer due to the presence of the horizontal bottom surfaces and a resulting rightward flow induced there with the same mechanism as that of thermal creep flow. Some simulations were reported using DUGKS; where the dependence of the mass flux on the wall temperature difference and Knudsen number are reported. We showed that mass flux is a nonlinear function of the temperature difference at moderate and high ΔT, and, as ΔT increases, the performance of case 7 enhances more compared to case 1. The least-square curve fit to the numerical predictions for the mass flux dependence on the *Kn* showed that different cases behave dissimilarly with *Kn* variations mainly because of the different structures of their produced temperature field.

Acknowledgements

Group	Case	L_{max}/λ	$\delta t/\delta t_{tr}$
1	1	0.1725	0.0180
	2	0.1085	0.0500
	3	0.1379	0.0428
2	4	0.1085	0.0508
	5	0.1379	0.0220
3	6	0.1385	0.0435
	7	0.1543	0.0590

TABLE 6. Cell size and time step in DSMC simulation test cases.

Grid	Cells	p_{avg} (10^{-2} atm)	ρ_{avg} (10^{-7} kg m^{-3})	T_{avg} (K)	$|U_{x_{avg}}|$ (m s^{-1})	$\hat{j}$ (10^{-2})
1	2592	2.209	1.672	445.591	32.638	7.000
2	3264	2.210	1.673	445.609	32.647	6.985
3	7344	2.210	1.673	445.584	32.666	6.971
4	9408	2.207	1.671	445.534	32.694	6.962

TABLE 7. Flow field properties at various cell sizes in DSMC simulations, PPC $= 20$.

Appendix A. Cell size and time step in DSMC simulations

Table 6 reports the ratio of the maximum cell size to the initial gas mean free path and simulation time step to the mean transit time for all investigated cases. In DSMC simulations, time step should be smaller than the mean collision time and mean transit time; the former is defined as:

$$\delta t_{coll} = \frac{\lambda}{U_{mp}}. \tag{A 1}$$

The transitional time step reads as:

$$\delta t_{tr} = \frac{L_{cell}}{U_{mp}}, \tag{A 2}$$

where L_{cell} is the minimum length of the cell. Evidently, fulfilment of the $\delta t/\delta t_{tr} < 1$ condition guarantees a time step smaller than the mean collision time.

Considering case 7 at $Kn = 0.9$, a detailed study of the grid size, PPC and time step effects on the accuracy of the DSMC solutions was performed. The obtained results, for the distribution of various flow properties over a vertical line connecting the middle troughs between the bottom and the top walls, are reported in figures 15–17 in this appendix. Tables 7, 8 and 9 report average flow field properties and normalized mass flux considering cell size, PPC and time step effects. The tables and figures clearly indicate that, within the considered ranges of grid size, PPC and time step, the flow field solution shows an almost negligible dependence on these numerical parameters.
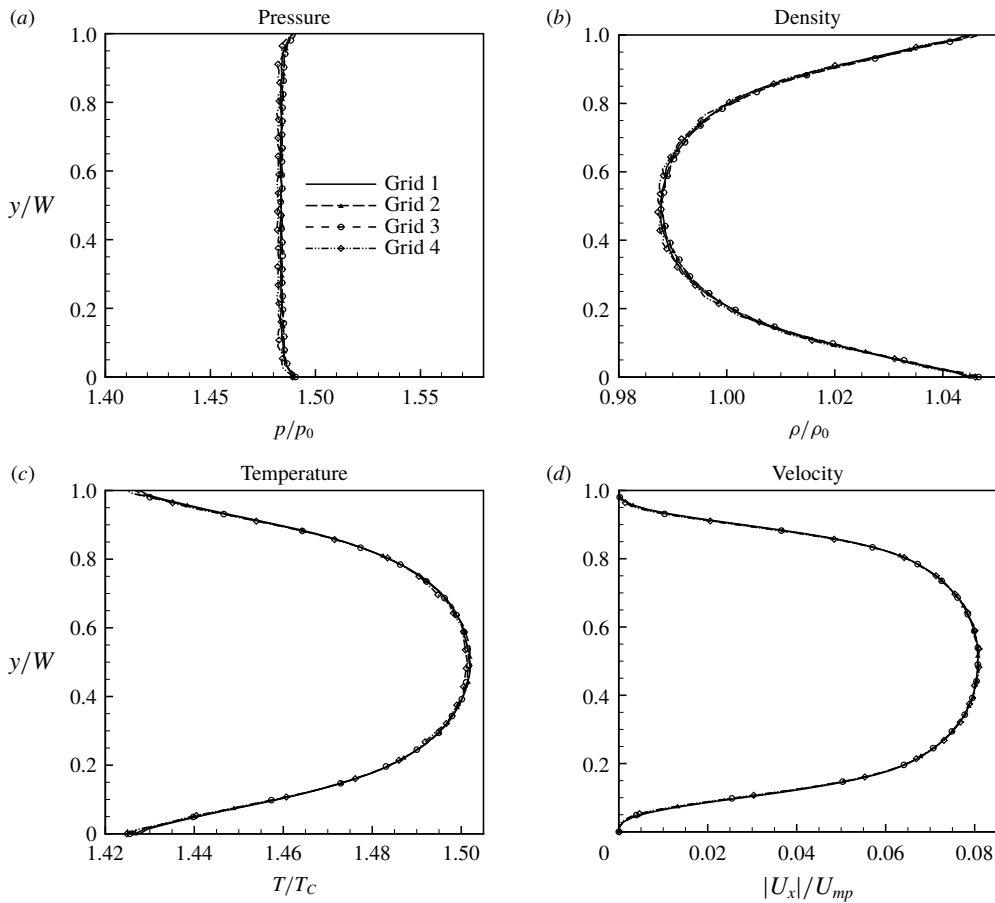
FIGURE 15. Grid dependence check for case 7, DSMC solutions.

PPC	p_{avg} $(10^{-2}$ atm)	ρ_{avg} $(10^{-7}$ kg m^{-3})	T_{avg} (K)	$|U_{x_{avg}}|$ (m s^{-1})	$\hat{j}$ (10^{-2})
10	2.209	1.672	445.604	32.657	6.984
20	2.210	1.673	445.609	32.647	6.985
40	2.208	1.672	445.553	32.659	6.984
80	2.208	1.672	445.477	32.617	6.974

TABLE 8. Dependence of flow field properties on the particle per cell in DSMC simulations, grid 2: 3264 cells.

Appendix B. Independence of DUGKS results from physical and velocity grid

In DUGKS, the particle velocity space is converted into a discrete velocity set. The discrete velocity set is selected as the abscissas of the desired quadrature rules such as the half-range Gauss–Hermite or compound Newton–Cotes rules, and the integrals over the velocity space in the DUGKS procedure are replaced by the quadrature.
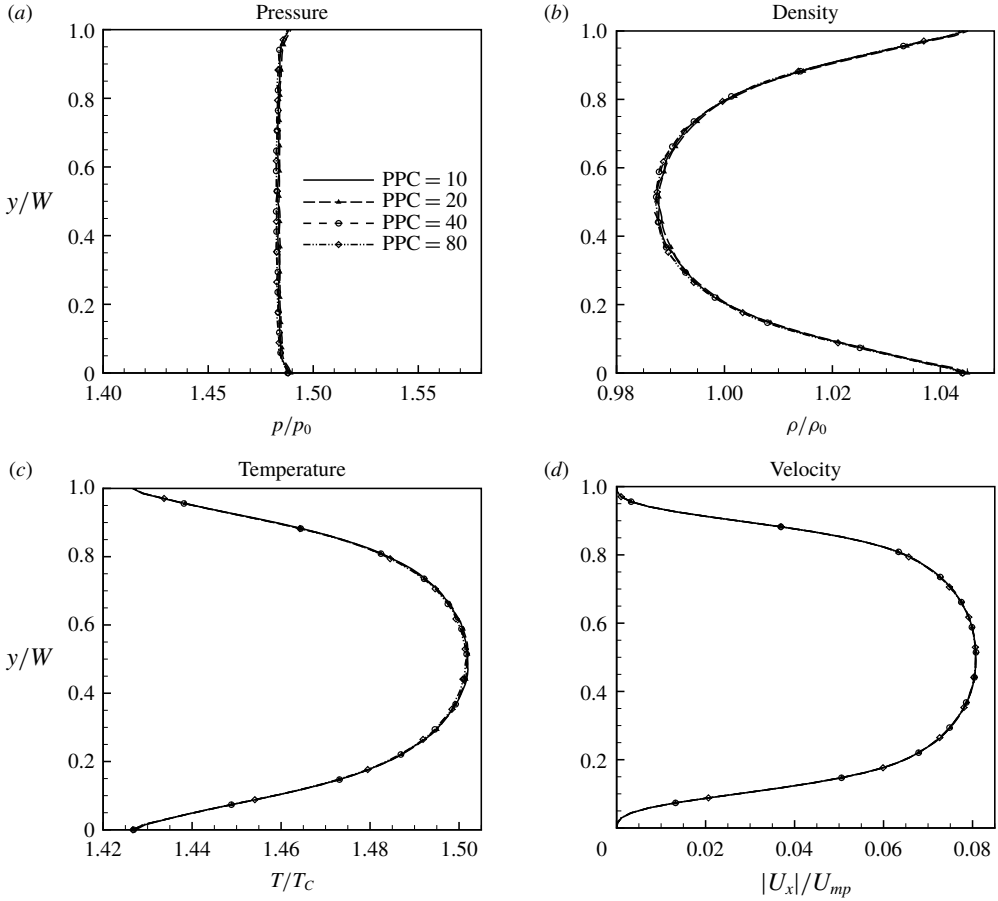
FIGURE 16. PPC dependence check for case 7, DSMC solutions.

$\delta t/\delta t_{tr}$	p_{avg} $(10^{-2}$ atm)	ρ_{avg} $(10^{-7}$ kg m$^{-3})$	T_{avg} (K)	$|U_{x_{avg}}|$ (m s^{-1})	$\hat{j}$ (10^{-2})
5.9×10^{-2}	2.205	1.669	445.577	32.670	6.973
5.9×10^{-3}	2.210	1.673	445.609	32.647	6.985
5.9×10^{-4}	2.207	1.671	445.641	32.536	6.952

TABLE 9. Dependence of flow field properties on the simulation time step in DSMC simulations, grid 2: 3264 cells, PPC $= 20$.

Case 7 was considered with various physical and velocity grids as well as quadrature rules. We changed the discrete velocity points from 28×28 to 41×41 and increased physical grids from 2232 to 6400 cells. The results presented in table 10 clearly indicate that the average axial velocity prediction of the coarsest physical/velocity grid (DUGKS-1) only deviates from the DSMC solution by less than 3.2 %. The deviation decreases if a fine grid is employed, e.g. the predicted
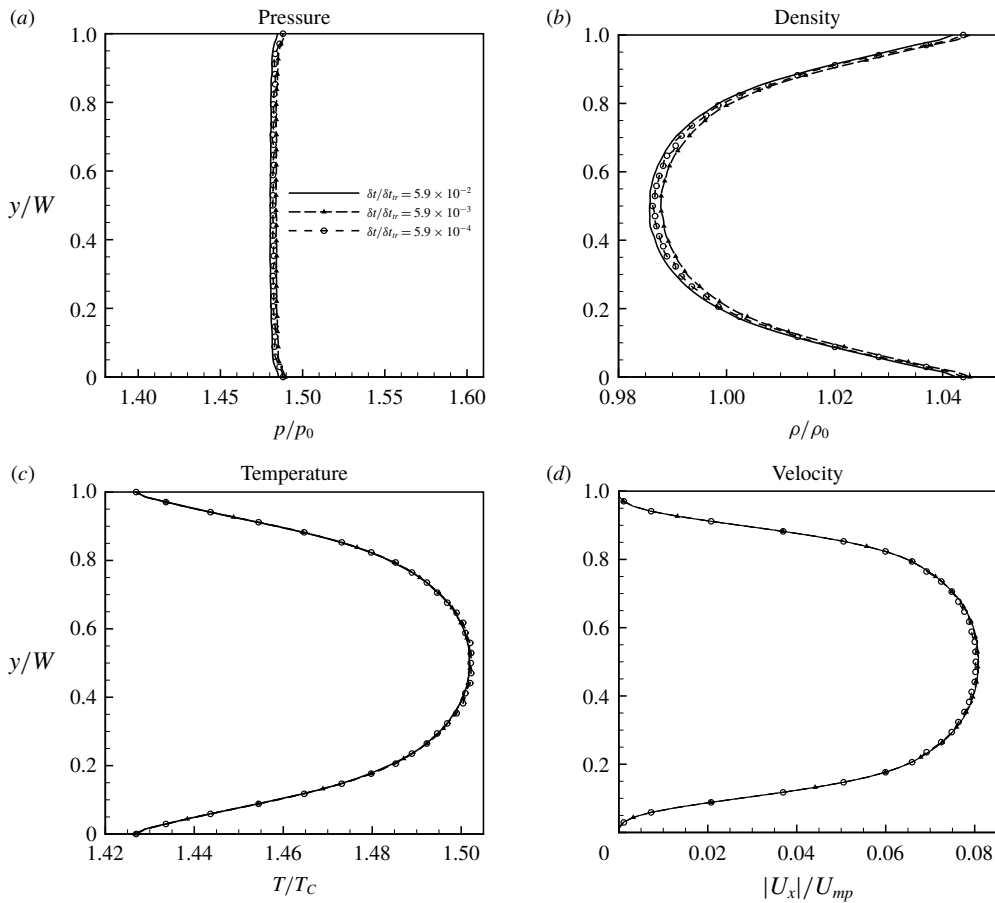
FIGURE 17. Time step dependence check for case 7, DSMC solutions.

Test case	Cells	Quadrature type	No. of points	T_{avg} (K)	$|U_{x_{avg}}|$ (m s^{-1})	$\hat{j}$ (10^{-2})
DUGKS-1	2232	Half-range Gauss–Hermite	28×28	446.809	33.594	7.194
DUGKS-2	4160	Half-range Gauss–Hermite	28×28	446.692	33.584	7.130
DUGKS-3	6400	Half-range Gauss–Hermite	28×28	446.697	33.552	7.123
DUGKS-4	2232	Compound Newton–Cotes	41×41	446.586	33.468	7.096
DUGKS-5	4160	Compound Newton–Cotes	41×41	446.495	33.433	7.075
DUGKS-6	6400	Compound Newton–Cotes	41×41	446.382	33.330	7.067
DSMC	7344	—	—	445.584	32.666	6.971

TABLE 10. Flow field properties for case 7 from DUGKS at various grid conditions at $Kn = \lambda/H = 0.9$.

axial velocity of case DUGKS-6 shows a 1.3 % deviation. In general, DUGKS shows a robust solution with respect to the grids and the integration scheme.

Table 11 reports quadrature type, number of cells, number of discrete velocity grid points and cell sizes employed for the results reported in the paper.

Case	Kn	Quadrature type	No. of points	No. of Cells
1	0.01, 0.1, 0.5	Half-range Gauss–Hermite	28×28	
	1, 2.5, 5	Compound Newton–Cotes	41×41	4820
	10	Compound Newton–Cotes	61×61	
7	0.01, 0.1, 0.5	Half-range Gauss–Hermite	28×28	
	0.9	Compound Newton–Cotes	41×41	
	2.5	Compound Newton–Cotes	61×61	4160
	5	Compound Newton–Cotes	81×81	
	10	Compound Newton–Cotes	121×121	

TABLE 11. Numbers of quadrature points in the velocity space, quadrature type and number of cells for different cases used in the DUGKS simulation reported in the paper.
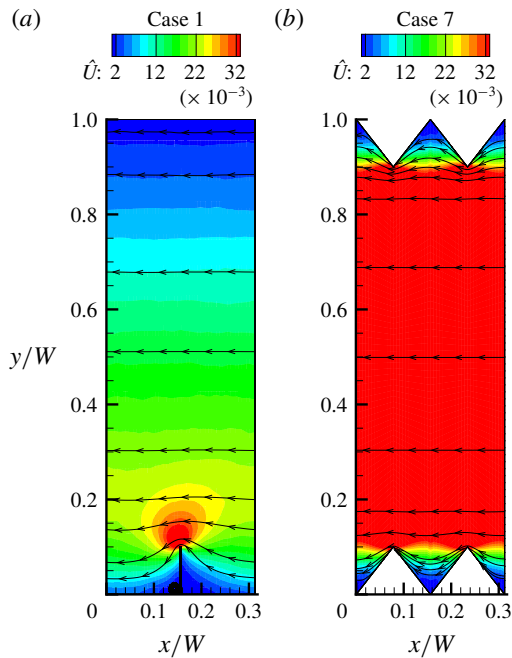

FIGURE 18. (Colour online) Isolines of the normalized velocity magnitude and streamlines from DSMC simulations, $\hat{U} = U/U_0$ at $Kn = 0.1$ for (*a*) case 1, (*b*) case 7.

Appendix C. Effect of Knudsen number on flow field structure

Most of the DSMC results presented in the body of the paper were obtained at $Kn \sim 0.9$–1. In this section, using DSMC, we consider the effect of a Kn variation on the flow and force patterns for cases 1 and 7 as typical test cases. Here, both cases were simulated at $Kn = \lambda/H = 0.1$. Figure 18 depicts normalized velocity contours for both cases at $Kn = 0.1$. Figure 19 compares the velocity distribution over a vertical line connecting the tip of the vane/ratchet to the top wall/tip of the ratchet in cases 1 and 7, respectively, at two investigated Knudsen numbers.

According to the force mechanism of radiometric flow, the flow becomes localized near the edge with a reduction in Kn. Thus, the flow grows stronger near the tips
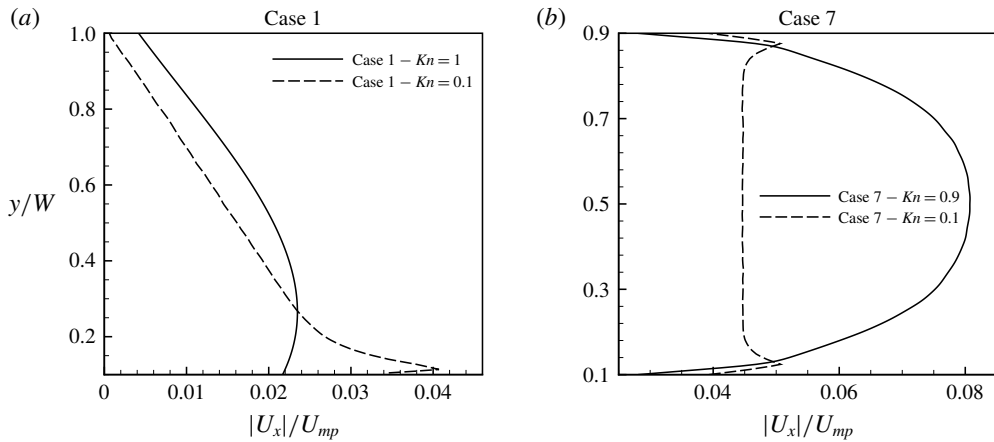
(a) Case 1

(b) Case 7

FIGURE 19. Comparison of the normalized velocity distribution over a vertical line connecting the tip of the vane/tooth and the top wall/tip of the tooth at two Knudsen numbers for (a) case 1, (b) case 7, DSMC solutions.
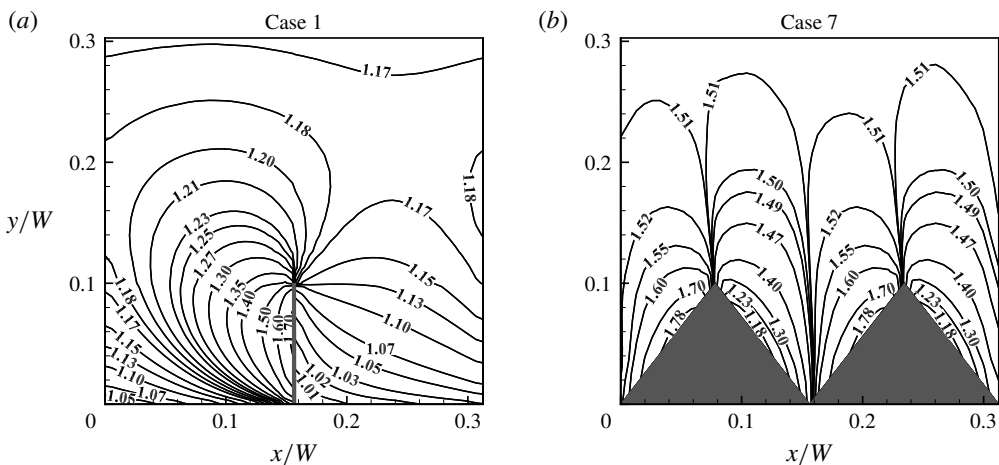
(a) Case 1

(b) Case 7

FIGURE 20. Isolines of the normalized temperature around the tip of the vane/ratchet at $Kn = 0.1$ for (a) case 1, (b) case 7, DSMC solutions.

compared to other regions in the simulation domain. Figure 19 shows that the maximum velocity of both cases occurs slightly above the tip regions at $Kn = 0.1$. Compared to the higher Kn conditions reported in the paper, the velocity profile of case 1 at $Kn = 0.1$ sharply decreases from above the tip region towards the top wall with a lower velocity slip on the top wall. Case 7 at $Kn = 0.1$, indeed, shows a uniform velocity profile in most parts of the channel far from the tip. As the flow is unidirectional and there are no imposed forces, such as a pressure gradient outside the Knudsen layer, a straight profile is expected. Except near the tips, this profile has a similar tendency to the thermal transpiration flow profile between two unpatterned plates at low Kn (Ohwada *et al.* 1989).

Figure 20 reports the temperature profile of both cases at $Kn = 0.1$. Temperature elevates above the vane with Kn diminution. With decreasing Kn, the temperature
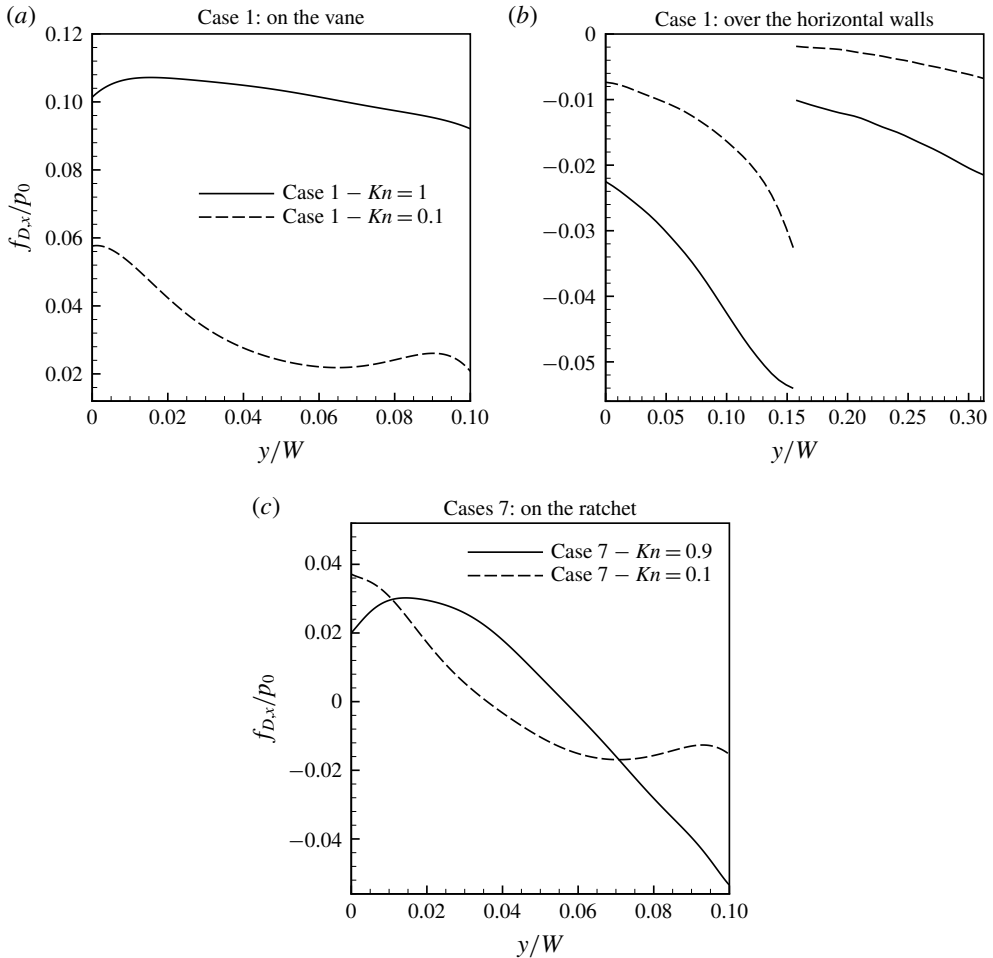
FIGURE 21. Comparison of normalized force at various Kn for $(a–b)$ case 1, (c) case 7, DSMC solutions.

jumps at the diffuse walls reduce, reflected by the presence of the isotherms of higher magnitude on the left side of the vane in figure 20 compared to the higher Kn condition reported in the paper.

The remarkable phenomenon in the velocity contours of case 1 at $Kn = 0.1$ is the existence of a small vortex attached to the vane at its left root, see figure 18(a). The vortex appeared due to the balance between the downward-moving radiometric flow and the rightward-moving flow on the left horizontal surface.

Considering figure 21($a–b$), which reports the force distribution on the vane and horizontal bottom wall at $Kn = 0.1$ and $Kn = 1$, it is concluded that the ratio of the radiometric force on the vane to the opposing shear stress force declined as Kn decreased. Accordingly, it is conceivable that a vortex appears on the root of the vane at $Kn = 0.1$. The reduction in Kn to 0.1 caused an obvious reduction in the force in the central section of the vane as molecular collisions degrade the area force generation. Figure 21(c) shows normalized force distribution in case 7. As previously discussed, the net force is zero in this case. This is correct for both lines depicted in this figure.

Case	Kn	p_{avg} (10^{-2} atm)	T_{avg} (K)	$|U_{x_{max}}|$ (m s^{-1})	$|U_{x_{avg}}|$ (m s^{-1})	$\hat{j}$ (10^{-2})	λ_{ave} (10^{-1} m)	F_x (10^{-4} N m^{-1})
1	0.1	14.66	334.76	20	6.83	1.571	0.40	1
	1	1.45	325.19	12	7.99	1.879	4.00	1.06
7	0.1	20.14	450.60	26	20.95	4.468	0.39	0
	0.9	2.21	445.59	40	32.64	6.985	3.60	0

TABLE 12. Comparison of DSMC predictions of flow field properties of cases 1 and 7 at two Kn conditions.

According to table 12, which reports the flow field properties of both cases at two Kn conditions, the net axial force on the vane is slightly lower at $Kn = 0.1$ compared to $Kn = 1$. Note that the average velocity is also smaller in the former, but the maximum velocity is approximately 5/3 times greater relative to that at $Kn = 1$, justifying a strong flow locality at lower Kn conditions. However, the gas density is higher at $Kn = 0.1$, resulting in a higher mass flux in this condition. Case 7, on the other hand, experiences lower mean and maximum velocities at $Kn = 0.1$ compared to the data previously reported in the manuscript at $Kn = 0.9$ for the same test case.

REFERENCES

AKHLAGHI, H., ROOHI, E. & STEFANOV, S. 2018 On the consequences of successively repeated collisions in no-time-counter collision scheme in DSMC. *Comput. Fluids* **161**, 23–32.

AOKI, K., DEGOND, P. & MIEUSSENS, L. 2009 Numerical simulations of rarefied gases in curved channels: thermal creep, circulating flow, and pumping effect. *Commun. Comput. Phys.* **6** (5), 919–954.

AOKI, K., SONE, Y., TAKATA, S., TAKAHASHI, K. & BIRD, G. 2001 One-way flow of a rarefied gas induced in a circular pipe with a periodic temperature distribution. In *Rarefied Gas Dynamics: 22nd International Symposium* (ed. T. J. Bartel & M. A. Gallis), pp. 940–947. AIP, Melville.

BAIER, T., HARDT, S., SHAHABI, V. & ROOHI, E. 2017 Knudsen pump inspired by Crookes radiometer with a specular wall. *Phys. Rev. Fluids* **2** (3), 033401.

BOND, D., WHEATLEY, V. & GOLDSWORTHY, M. 2016 Numerical investigation into the performance of alternative Knudsen pump designs. *Intl J. Heat Mass Transfer* **93**, 1038–1058.

CHEN, J., STEFANOV, S. K., BALDAS, L. & COLIN, S. 2016 Analysis of flow induced by temperature fields in ratchet-like microchannels by Direct Simulation Monte Carlo. *Intl J. Heat Mass Transfer* **99**, 672–680.

CORNELLA, B. M., KETSDEVER, A. D., GIMELSHEIN, N. E. & GIMELSHEIN, S. F. 2012 Analysis of multivane radiometer arrays in high-altitude propulsion. *J. Propul. Power* **28** (4), 831–839.

CROOKES, W. 1874 XV. On attraction and repulsion resulting from radiation. *Phil. Trans. R. Soc. Lond.* A **164**, 501–527.

DONKOV, A. A., TIWARI, S., LIANG, T., HARDT, S., KLAR, A. & YE, W. 2011 Momentum and mass fluxes in a gas confined between periodically structured surfaces at different temperatures. *Phys. Rev.* E **84** (1), 016304.

GIMELSHEIN, N., GIMELSHEIN, S., KETSDEVER, A. & SELDEN, N. 2011a Impact of vane size and separation on radiometric forces for microactuation. *J. Appl. Phys.* **109** (7), 074506.

GIMELSHEIN, N. E., GIMELSHEIN, S. F., KETSDEVER, A. D. & SELDEN, N. P. 2011b Shear force in radiometric flows. In *Rarefied Gas Dynamics: 27th International Symposium* (ed. D. A. Levin, I. J. Wysong & A. L. Garcia), AIP Conference Proceedings, vol. 1333, pp. 661–666.

GUO, Z., WANG, R. & XU, K. 2015 Discrete unified gas kinetic scheme for all Knudsen number flows. II. Thermal compressible case. *Phys. Rev.* E **91** (3), 033313.

KETSDEVER, A., GIMELSHEIN, N., GIMELSHEIN, S. & SELDEN, N. 2012 Radiometric phenomena: from the 19th to the 21st century. *Vacuum* **86** (11), 1644–1662.

NALLAPU, R. T., TALLAPRAGADA, A. & THANGAVELAUTHAM, J. 2017 Radiometric actuators for spacecraft attitude control. arXiv:1701.07545.

OHWADA, T., SONE, Y. & AOKI, K. 1989 Numerical analysis of the Poiseuille and thermal transpiration flows between two parallel plates on the basis of the Boltzmann equation for hard-sphere molecules. *Phys. Fluids* A **1** (12), 2042–2049.

PALHARINI, R. C., WHITE, C., SCANLON, T. J., BROWN, R. E., BORG, M. K. & REESE, J. M. 2015 Benchmark numerical simulations of rarefied non-reacting gas flows using an open-source DSMC code. *Comput. Fluids* **120**, 140–157.

ROOHI, E. & STEFANOV, S. 2016 Collision partner selection schemes in DSMC: From micro/nano flows to hypersonic flows. *Phys. Rep.* **656**, 1–38.

ROOHI, E., STEFANOV, S., SHOJA-SANI, A. & EJRAEI, H. 2018 A generalized form of the Bernoulli Trial collision scheme in DSMC: derivation and evaluation. *J. Comput. Phys.* **354**, 476–492.

SCANLON, T., ROOHI, E., WHITE, C., DARBANDI, M. & REESE, J. 2010 An open source, parallel DSMC code for rarefied gas flows in arbitrary geometries. *Comput. Fluids* **39** (10), 2078–2089.

SELDEN, N., NGALANDE, C., GIMELSHEIN, N., GIMELSHEIN, S. & KETSDEVER, A. 2009 Origins of radiometric forces on a circular vane with a temperature gradient. *J. Fluid Mech.* **634**, 419–431.

SHAHABI, V., BAIER, T., ROOHI, E. & HARDT, S. 2017 Thermally induced gas flows in ratchet channels with diffuse and specular boundaries. *Sci. Rep.* **7**, 41412.

STEFANOV, S. K. 2011 On DSMC calculations of rarefied gas flows with small number of particles in cells. *SIAM J. Sci. Comput.* **33** (2), 677–702.

STRONGRICH, A., PIKUS, A., SEBASTIÃO, I. B. & ALEXEENKO, A. 2017 Microscale in-plane knudsen radiometric actuator: design, characterization, and performance modeling. *J. Microelectromech. Syst.* **26** (3), 528–538.

SU, C., TSENG, K., CAVE, H., WU, J., LIAN, Y., KUO, T. & JERMY, M. 2010 Implementation of a transient adaptive sub-cell module for the parallel-DSMC code using unstructured grids. *Comput. Fluids* **39** (7), 1136–1145.

TAGUCHI, S. & AOKI, K. 2012 Rarefied gas flow around a sharp edge induced by a temperature field. *J. Fluid Mech.* **694**, 191–224.

TAGUCHI, S. & AOKI, K. 2015 Motion of an array of plates in a rarefied gas caused by radiometric force. *Phys. Rev.* E **91** (6), 063007.

TAKATA, S. & FUNAGANE, H. 2013 Singular behaviour of a rarefied gas on a planar boundary. *J. Fluid Mech.* **717**, 30–47.

VARGO, S., MUNTZ, E., SHIFLETT, G. & TANG, W. 1999 Knudsen compressor as a micro-and macroscale vacuum pump without moving parts or fluids. *J. Vac. Sci. Technol.* A **17** (4), 2308–2313.

WHITE, C., BORG, M., SCANLON, T., LONGSHAW, S., JOHN, B., EMERSON, D. & REESE, J. 2018 dsmcFoam+: an OpenFOAM based direct simulation Monte Carlo solver. *Comput. Phys. Commun.* **224**, 22–43.

WHITE, C., BORG, M. K., SCANLON, T. J. & REESE, J. M. 2013 A DSMC investigation of gas flows in micro-channels with bends. *Comput. Fluids* **71**, 261–271.

ZHU, L., CHEN, S. & GUO, Z. 2017 dugksFoam: an open source OpenFOAM solver for the Boltzmann model equation. *Comput. Phys. Commun.* **213**, 155–164.

ZHU, L. & GUO, Z. 2017*a* Application of discrete unified gas kinetic scheme to thermally induced nonequilibrium flows. *Comput. Fluids* (in press).

ZHU, L. & GUO, Z. 2017*b* Numerical study of nonequilibrium gas flow in a microchannel with a ratchet surface. *Phys. Rev.* E **95** (2), 023113.